MNRAS 000, 1–21 (2018) Preprint 19 November 2018 Compiled using MNRAS LATEX style file v3.0

Early-type galaxy density profiles from IllustrisTNG: I. Galaxy correlations and the impact of baryons

Yunchong Wang[1,2⋆], Mark Vogelsberger[1], Dandan Xu[3,2], Shude Mao[2,4,5], Volker Springel[6], Hui Li[1], David Barnes[1], Lars Hernquist[7], Annalisa Pillepich[8], Federico Marinacci[7], Rüediger Pakmor[9], Rainer Weinberger[7] and Paul Torrey[10]

[1] *Kavli Institute for Astrophysics and Space Research, Department of Physics, MIT, Cambridge, MA 02139, USA*
[2] *Tsinghua Center for Astrophysics, Department of Physics, Tsinghua University, Beijing, 100084, China*
[3] *Institute for Advanced Studies, Tsinghua University, Beijing, 100084, China*
[4] *National Astronomical Observatories, Chinese Academy of Sciences, Beijing, 100012, China*
[5] *Jodrell Bank Centre for Astrophysics, The University of Manchester, Alan Turing Building, Manchester M13 9PL, UK*
[6] *Max-Planck-Institut für Astrophysik, Karl-Schwarzschild-Str. 1, D-85748, Garching, Germany*
[7] *Harvard-Smithsonian Center for Astrophysics, 60 Garden Street, Cambridge, MA 02138*
[8] *Max-Planck-Institut für Astronomie, Königstuhl 17, 69117 Heidelberg, Germany*
[9] *Heidelberg Institute for Theoretical Studies, Schloss-Wolfsbrunnenweg 35, D-69118 Heidelberg, Germany*
[10] *Department of Astronomy, University of Florida, 211 Bryant Space Sciences Center, Gainesville, FL 32611, USA*

arXiv:1811.06545v1 [astro-ph.GA] 15 Nov 2018

Accepted ***. Received ***; in original form ***

ABSTRACT

We explore the isothermal total matter radial density profiles in early-type galaxies (ETGs) selected from the IllustrisTNG simulation. For a sample of 514 ETGs in the stellar mass range of $10^{10.7}\mathrm{M}_\odot \leqslant M_* \leqslant 10^{11.9}\mathrm{M}_\odot$ at $z = 0$, the total power-law slope has a mean of $\langle\gamma'\rangle = 2.003 \pm 0.008$ and a standard deviation of $\sigma_{\gamma'} = 0.175$ over the radial range from 0.4 to 4 times the stellar half mass radius. Several correlations between γ' and galactic properties including stellar mass, effective radius, stellar surface density, central velocity dispersion, central dark matter fraction and in-situ-formed stellar mass ratio are compared to observations and other simulations, revealing that IllustrisTNG reproduce correlation trends qualitatively, and γ' is almost constant with redshift below $z = 2$. The power-law density profile of the ETG dark matter halos is steeper in the full physics (FP) run than their counterparts in the dark matter only (DMO) run. The dark matter inner slopes of the best-fit generalized NFW profile are much steeper than the standard NFW profile and they are anti-correlated (constant) with the halo mass in the FP (DMO) run. The dark matter inner slope is also anti-correlated with the halo concentration parameter c_{200} in both runs. Comparison of the mass-weighted slope/central dark matter fraction correlation, $\gamma'_{\mathrm{mw}}-f_{\mathrm{DM}}$, with models and observations indicates contraction of the IllustrisTNG dark matter halos, especially in lower-mass systems.

Key words: galaxies: formation – galaxies: structure – cosmology: theory – dark matter – methods: numerical

1 INTRODUCTION

The general structure formation scenario of the Universe in the Λ-Cold Dark Matter (CDM) cosmology model consists of a 'bottom up' assembly of dark matter halos and subsequent gas cooling and star formation leading to the formation of the galaxies we see today (e.g. White & Rees 1978; Blumenthal et al. 1984; Cole et al. 1994). This scenario has been tested robustly by semi-analytical modeling (Kauffmann et al. 1993; Baugh et al. 1999; Cole et al. 2000), N-body numerical simulations (Davis et al. 1985; Springel et al. 2005) and cosmological hydrodynamic simulations (Vogelsberger et al. 2014a,b; Dubois et al. 2014; Schaye et al. 2015) over the past few decades.

Early-type galaxies (hereafter, ETGs) are massive elliptical and lenticular galaxies with little gas and old stellar populations. As final products of galaxy mergers and secular formation processes, they provide crucial insights for

⋆ E-mail: ycwang15@mit.edu

© 2018 The Authors

testing and constraining the theory of structure formation within their large-scale cosmological environment. Over the past decade, the joint efforts of many galaxy surveys have resulted in a significant sample of observed ETGs, including strong lensing surveys such as the Lensing Structure and Dynamics Survey (Treu & Koopmans 2002; Koopmans & Treu 2003; Treu & Koopmans 2004, LSD), the Sloan Lens ACS Survey (Bolton et al. 2006; Treu et al. 2006; Auger et al. 2009, SLACS), the Strong Lensing Legacy Survey (Cabanac et al. 2007; Gavazzi et al. 2012, SL2S), the BOSS Emission-Line Lens Survey (Bolton et al. 2012; Brownstein et al. 2012, BELLS), and surveys targeted at stellar kinematics and dynamics such as SPIDER (La Barbera et al. 2010), ATLAS^{3D} (Cappellari et al. 2011), the SLUGGS Survey (Brodie et al. 2014; Forbes et al. 2016), and the MASSIVE Survey (Ma et al. 2014). Through detailed stellar dynamics and strong lensing modeling, the masses, sizes, stellar and total density distributions and other dynamical features of ETGs are constrained to different levels.

Interestingly, the average total power-law density slope of observed ETGs has been found to be close to isothermal within a few effective radii, i.e., $\rho(r) \propto r^{-\gamma'}$, where $\gamma' = 2$, which describes a sphere of collisional ideal gas in equilibrium between thermal pressure and self gravity. This coincidence sometimes is also referred to as the 'bulge-halo conspiracy': while neither the stellar- (baryonic-) component nor the dark matter halo exhibits an isothermal density distribution, the sum of the two appears to follow such a profile with little intrinsic scatter. The observational evidence for the presence of near-isothermal density profiles in ETGs is prevalent and convincing, from dynamically modeled ETGs at $z \approx 0$ (Tortora et al. 2014; Serra et al. 2016; Poci et al. 2017; Bellstedt et al. 2018), strong lensing ETGs which trace back to $z = 1$ (Koopmans et al. 2006, 2009; Barnabè et al. 2009, 2011; Auger et al. 2010b; Ruff et al. 2011; Sonnenfeld et al. 2013; Lyskova et al. 2018), and X-ray observations of ETGs (Humphrey et al. 2006; Humphrey & Buote 2010). Apart from the near-isothermal behavior, the total density profiles of observed ETGs also show clear correlations with galaxy parameters, such as the total stellar mass, effective radius, stellar surface density, central velocity dispersion and central dark matter fraction (Auger et al. 2010b; Sonnenfeld et al. 2013; Newman et al. 2015; Poci et al. 2017). A mild shallowing trend of the total density profile with increasing redshift is also observed (Koopmans et al. 2006; Auger et al. 2010b; Barnabè et al. 2011; Ruff et al. 2011; Sonnenfeld et al. 2013).

Dedicated theoretical studies including semi-analytical modeling and simulations, aiming at explaining the 'bulge-halo conspiracy', have converged on a scenario in which ETGs form in a two-stage fashion: dissipative gas cooling first triggers active star formation and dark matter halo contraction which steepens the density profile, then non-dissipative mergers and accretion follow and make the density profile shallower (Naab et al. 2007; Nipoti et al. 2009a,b; Hopkins et al. 2009; Kormendy et al. 2009; Johansson et al. 2012; Dubois et al. 2013; Remus et al. 2013; Rodriguez-Gomez et al. 2015). This is in line with the constraints from the more profound ETG scaling laws, such as the fundamental plane relations (Faber et al. 1987; Jorgensen et al. 1996; Cappellari et al. 2006; Robertson et al. 2006a) and the $M_{\rm BH} - \sigma_{\rm v}$ relation (Ciotti & van Albada 2001; Pinkney et al. 2003; Robertson et al. 2006b; Graham 2008; McConnell & Ma 2013), which also indicate the important role of dissipative processes. Although ETG evolution is dominated by 'dry' mergers, Sonnenfeld et al. (2014) claimed dissipative 'wet' mergers are indispensable in addition to 'dry' mergers during the formation of ETGs in order to establish the observed redshift evolution of the ETG density profile. These efforts were crucial steps towards a self-consistent ETG formation and evolution scenario, bridging the gap between theoretical assumptions and observational uncertainties.

Furthermore, since the 'bulge-halo conspiracy' emphasizes the interplay between baryonic and dark matter components that comprise the ETGs, it is of critical importance to study the individual effects of baryons and dark matter. Conventionally, the dark matter halo profile is believed to be universally well-described by an NFW profile (Navarro et al. 1997). However, recent studies from observations (Auger et al. 2010a; Treu et al. 2010) and simulations (Navarro et al. 2010; Hjorth et al. 2015; Chua et al. 2017) have revealed that the dark matter profile is in fact non-universal, and the influence of baryonic processes on dark matter halos varies with halo size, shape and environment (Governato et al. 2010; Newman et al. 2013; Chua et al. 2018). The observed dark matter halo contraction (Sonnenfeld et al. 2012; Grillo 2012; Oguri et al. 2014; Newman et al. 2015; Bruderer et al. 2016) is in agreement with mild contraction models (Gnedin et al. 2004; Abadi et al. 2010), ruling out adiabatic contraction (Blumenthal et al. 1986), and is consistent with the weak dissipative processes predicted by the theoretical studies noted above in shaping ETG density profiles. This has been shown to be true for IllustrisTNG elliptical galaxies at $z = 0$ compared to observations, and some tension in the contraction level still exists at $z = 2$ (Lovell et al. 2018).

With the advent of a new generation of cosmological hydrodynamic simulations, i.e. the Illustris simulations[1] (Vogelsberger et al. 2014a,b; Genel et al. 2014; Sijacki et al. 2015; Nelson et al. 2015), the EAGLE Project[2] (Schaye et al. 2015; Crain et al. 2015), and the Magneticum Pathfinder[3] simulations (Dolag et al. to be submitted), large statistical samples of simulated ETGs have become available that reproduce the observed density profiles and correlation trends (e.g. see Remus et al. 2017; Xu et al. 2017; Barber et al. 2018 and references therein). In this paper, we use the IllustrisTNG project[4] (Marinacci et al. 2018; Naiman et al. 2018; Nelson et al. 2018; Pillepich et al. 2018b; Springel et al. 2018), an updated set of simulations with a new physical model extending the original Illustris project, and select a realistic sample of simulated ETGs to study the statistical properties and correlations with global galactic properties of their density profiles. We will: **a)** investigate the distribution of the total density slopes in different radial ranges; **b)** compare the correlations between the simulated total density slopes with a number of galaxy properties as well as the redshift evolution of the slopes with a diverse dataset from observations and other simulations to explore the outcome

[1] http://www.illustris-project.org/
[2] http://icc.dur.ac.uk/Eagle/
[3] http://www.magneticum.org/
[4] http://www.tng-project.org

and systematic biases of our IllustrisTNG ETG sample; **c)** compare between full physics and dark matter only simulations to elucidate the impact of baryons in shaping density profiles of the total and dark matter components.

This paper is organized as follows: in Section 2 we briefly introduce the IllustrisTNG simulations, our sample selection criteria and the post-processing tools that we use for our analysis; in Section 3 we present the measured total power-law density slopes of the IllustrisTNG ETG samples and their correlations with a number of global galactic properties as well their redshift evolution; in Section 4 we describe the difference between the full physics simulation and the dark matter only simulation to identify the separate contributions of baryonic and dark matter in the origin of the density profiles; in Section 5 we summarize the general properties we obtained for the IllustrisTNG ETGs in this work and discuss further questions that still need to be answered in the future. Throughout this paper, we adopt the Planck ΛCDM cosmology (Planck Collaboration et al. 2016), which is also used in the IllustrisTNG simulations; i.e., $h = 0.6774$, $\Omega_{\rm m} = 0.3089$, $\Omega_\Lambda = 0.6911$, $\Omega_{\rm b} = 0.0486$, and $\sigma_8 = 0.8159$.

The full dataset of the IllustrisTNG ETGs that we present in this work will be available on the IllustrisTNG website (http://www.tng-project.org/).

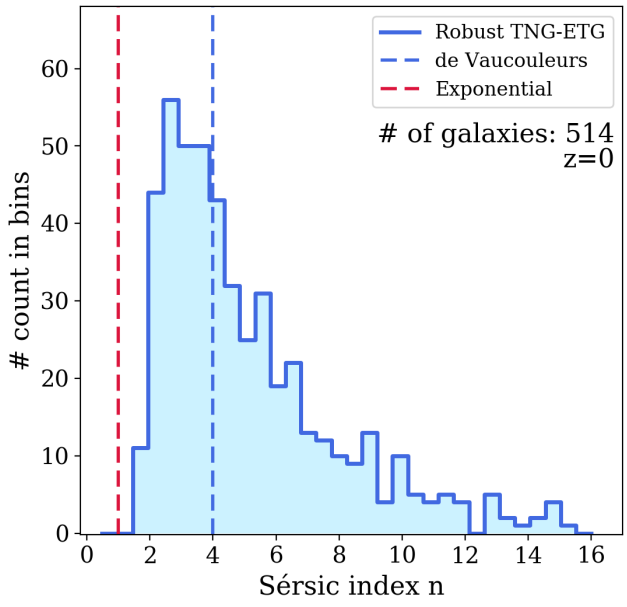

Figure 1. The distribution of the Sérsic index of the single Sérsic model fitted to our final sample of 514 $z = 0$ IllustrisTNG ETGs. The blue solid histogram indicates the number distribution of our selected IlustrisTNG ETGs, and they typically have Sérsic index $n \geqslant 2$, which well represents the luminosity profiles of an ETG sample.

2 METHODOLOGY

2.1 The simulation

The IllustrisTNG project (IllustrisTNG hereafter, see Marinacci et al. 2018; Naiman et al. 2018; Nelson et al. 2018; Pillepich et al. 2018b; Springel et al. 2018) is a suite of state-of-the-art magneto-hydrodynamic cosmological simulations. Evolved using the moving mesh hydrodynamics code AREPO (Springel 2010), the simulations were built upon the many successes of the original Illustris project (Vogelsberger et al. 2014a,b; Genel et al. 2014; Sijacki et al. 2015; Nelson et al. 2015) and the Illustris models (Vogelsberger et al. 2013; Torrey et al. 2014), but with improved prescriptions for both stellar and AGN feedback (Weinberger et al. 2017; Pillepich et al. 2018a). The full physics IllustrisTNG simulation suite reproduces many key relations in observed galaxies, including the galaxy-color bimodality in the Sloan Digital Sky Survey (Nelson et al. 2018), the evolution of the mass-metallicity relation (Torrey et al. 2017, 2018), the galaxy size-mass relation evolution (Genel et al. 2018), the fraction of dark matter within galaxies at $z = 0$ (Lovell et al. 2018), the intra-cluster metal distribution in galaxy clusters (Vogelsberger et al. 2018), and the cool-core structure in galaxy clusters (Barnes et al. 2018). These verifications of the IllustrisTNG physics model stand as strong confirmation of the plausibility of the simulated IllustrisTNG galaxy and galaxy cluster populations.

In this work we make use of the highest resolution version of the TNG100 simulation, which employs 2×1820^3 resolution elements in a $(75/h \approx 110.7\ {\rm Mpc})^3$ box. The baryonic and dark matter mass resolutions are $m_{\rm baryon} = 1.4 \times 10^6 {\rm M}_\odot$ and $m_{\rm DM} = 7.5 \times 10^6 {\rm M}_\odot$, respectively. A softening length of $\epsilon = 0.74\,{\rm kpc}$ (below $z = 1$) is adopted for the dark matter and stellar components, while the gravitational softening of the gas cells is fully adaptive (minimum 0.19 comoving kpc). We also make use of the TNG100-dark matter only (DMO) simulation, which has the same initial conditions, total mass and softening length as the TNG100-full physics run. The dark matter resolution in the DMO run is $m_{\rm DM} = 8.9 \times 10^6 {\rm M}_\odot$.

2.2 Galaxy classification and sample selection

Galaxy type classification is achieved using the same procedure as in Xu et al. (2017). Here we only briefly summarize the key steps and features involved.

Galaxies are identified as gravitationally bound structures of dark matter particles, stellar particles and gas elements, using the SUBFIND algorithm (Springel et al. 2001; Dolag et al. 2009). To derive the optical light of galaxies, each stellar particle is assigned a brightness magnitude in a given observational filter band based on its star formation age and metallicity using Bruzual & Charlot (2003) stellar population synthesis (SPS) model GALAXEV. A simple projection-dependent dust attenuation model is adopted in a post-processing fashion in order to take into account dust absorption and scattering effects.

Using the SDSS r-band rest-frame luminosity, we fit both a single de Vaucouleurs profile (de Vaucouleurs 1948) and a single exponential profile to a galaxy's radial surface brightness distribution in a given projection, for example X projection along the simulation box. As our first criterion, if a galaxy can be better fitted by the former than the latter (i.e., with a smaller χ^2), then it is classified as an ETG.

In addition, we also fit a combined de Vaucouleurs profile plus a Sérsic profile (Sérsic 1963) to the total radial light profile in order to describe a combined light distribution from both the galactic bulge and the disk components. As

our second criterion, if the integrated luminosity fraction of the de Vaucouleurs component is larger than half, then the galaxy is classified as an ETG.

In our final ETG sample, we only include galaxies whose radial light profiles in all three independent projections (along X, Y, and Z axes of the simulation box) satisfy both criteria above. In order to compare with the results from observations and other simulations (see Section 3.2 for details), we also select only *central* galaxies (the largest substructure identified by the SUBFIND algorithm in each FoF group) with total stellar mass $5 \times 10^{10} \mathrm{M}_{\odot} \leqslant M_{*} \leqslant 8 \times 10^{11} \mathrm{M}_{\odot}$ (about 3.6×10^{4} to 5.8×10^{5} stellar particles). Our selection criteria results in 514 well-resolved early-type galaxies at redshift $z = 0$, and 673 at $z = 0.2$, which are used to compare with local and higher-redshift ETG samples from both observations and other simulations.

To demonstrate the robustness of our final ETG sample, we present Fig. 1, which shows the histogram of the Sérsic index measured for 514 $z = 0$ galaxies (in their X-projection) in our final IllustrisTNG ETG sample. As shown in the figure, our selected IllustrisTNG ETGs typically have Sérsic index $n \geqslant 2$, representing the luminosity profiles of observed ETG samples.

2.3 Analysis

An exact power-law model $\rho(r) \propto r^{-\gamma'}$ provides a reasonable approximation to the total radial density profile of a given galaxy. In practice, whether in observation or simulation, the slope index γ' of an approximate power-law is always measured within a given radial range (r_1, r_2), usually from about a tenth the galaxy effective radius out to a few effective radii (see Section 3.2 for details). For each galaxy in our IllustrisTNG ETG sample, we adopt the position of the particle with the minimum gravitational potential in its host halo as the center of the galaxy. Assuming spherical symmetry, we calculate the total radial density distribution in 100 radial bins, equally divided in logarithmic scale. We then perform a linear fit (with equal radial weighting) to $\log \rho(r) - \log r$ within a given radial interval (r_1, r_2) and define the best linear fit slope as the power-law density slope γ' for the total radial density distribution. Although the observational modeling techniques implemented for deriving the power-law slopes involve various assumptions, the quantitative analysis of their systematic biases is beyond the scope of this paper. Therefore, we make direct comparison of the 'true' 3D power-law slope of the total mass density profile of the IllustrisTNG ETGs with the observational power-law slopes; i.e. we do not attempt to mock the observational procedures to derive γ'.

We further study the correlations between the power-law slope γ' and the following galaxy properties: total stellar mass, effective radius, stellar surface density, central velocity dispersion, stellar orbital anisotropy, central dark matter fraction and in-situ-formed stellar mass ratio. **i)** The total stellar mass M_{*} of an ETG is defined as the sum of the mass of all the stellar particles assigned to the ETG by SUBFIND within a 3D aperture of 30 kpc. **ii)** The 2D projected half light radius of the IllustrisTNG quenched galaxies has been shown to agree with observations within error bars, assuming 0.25 dex observational uncertainty in the measurement of stellar mass (Genel et al. 2018). However, different assumed stellar mass uncertainties, luminosity fitting methods, dust attenuation models, aperture size and shape, and projection effects all add up to the systematic biases in the size measurement. Therefore, we approximate the effective radius R_{eff} for an IllustrisTNG ETG by its 3D stellar half mass radius $R_{1/2}$ as calculated by SUBFIND, which is a model-independent size measurement intrinsic to the simulated galaxies. We apply this size approximation for IllustrisTNG ETGs throughout this paper. **iii)** The stellar surface density is defined as $\Sigma_{*} = M_{*}/2\pi R_{\mathrm{eff}}^{2}$. **iv)** The central velocity dispersion $\sigma_{\mathrm{e}/2}$ is calculated for all the stellar particles projected (along the X-projection of the simulation box) within the central 1/2 of the stellar half mass radius, with each stellar particle weighted by its (rest-frame) SDSS r-band luminosity. In addition, we also calculate the stellar orbital anisotropy parameter β, which is defined for all the stellar particles within the central 3D stellar half mass radius, each stellar particle weighted by its mass. **v)** The central dark matter fraction f_{DM} is calculated as the fraction of dark matter mass over the total mass of all dark matter, stellar and gas particles projected (along the X-projection) within the central 1/2 of the stellar half mass radius. **vi)** The in-situ-formed stellar mass ratio $f_{\mathrm{in-situ}}$ is the sum of all the stellar particles formed within the main progenitor branch of the ETG versus the total stellar mass of the ETG, using the stellar assembly catalogs derived for the galaxy version of the SUBLINK merger tree (Rodriguez-Gomez et al. 2015).

3 STATISTICAL PROPERTIES

In this section, we present the results for the total power-law density slope γ' of our selected ETG sample. It is found that the profiles are indeed close to isothermal with little intrinsic scatter. Further comparison to observations and other simulations reveals that the IllustrisTNG ETGs also show consistently tight correlations between global galactic properties and the total power-law density slope. The redshift evolution of γ' of the IllustrisTNG ETGs is almost constant below $z = 1$ and increases with increasing redshift above $z = 1$.

3.1 IllustrisTNG ETG total density slopes at $z = 0$

Fig. 2 presents the radial density distributions of the total (green) as well as dark matter (black), star (blue) and gas (red) of an example IllustrisTNG ETG. The best power-law fits to their total density profiles are given by the dashed lines of the same color. Obviously, the total, stellar and dark matter components are well-described by power-law models in the radial range $[0.4\,R_{1/2},\ 4\,R_{1/2}]$. The stellar component profile has a steeper slope than the total density profile, while the dark matter component profile has a shallower slope than the total density profile. The stellar component dominates over the gas component, which is characteristic of gas-poor early-type galaxies.

The presence and prevalence of isothermal density profiles in the inner region of ETGs has already been demonstrated in the original Illustris simulation (Xu et al. 2017). For the IllustrisTNG ETG sample, we follow the analysis method described in Section 2.3 to calculate each galaxy's total power-law density slope γ' within different radial

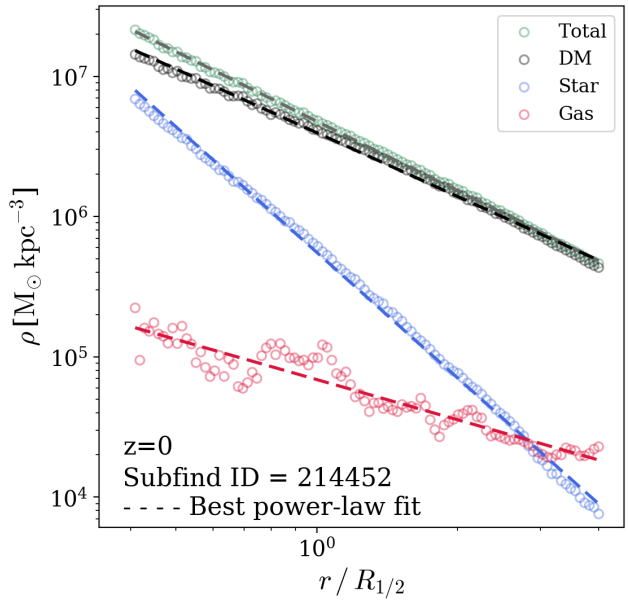

Figure 2. An illustration of a selected IllustrisTNG ETG 3D radial density profile in the radial range of $[0.4\,R_{1/2}, 4.0\,R_{1/2}]$, where $R_{1/2}$ is the 3D stellar half mass radius. The green, black, blue, and red open circles represent the 3D density of the total, dark matter, star and gas components, respectively. The best linear fit to the density components are depicted by the dashed lines with the same color. The slopes of all the components vary little over the range of $[R_{1/2}, 4\,R_{1/2}]$, and the dominance of dark matter increases with the increase of the outer radial range, which accounts for the weak evolution of $\langle\gamma'\rangle$ and the decrease in $\sigma_{\gamma'}$ across this radial range.

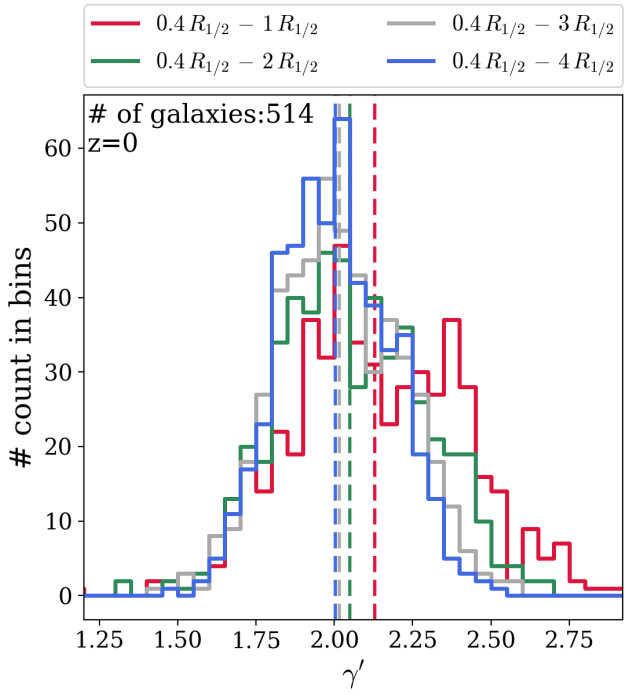

Figure 3. The total power-law density slope distribution of all 514 ETGs selected from IllustrisTNG at $z = 0$. Different colors represent the distribution of the total density slope in the radial range indicated in the legend. Each histogram with a certain color represents the number distribution of the total density slope measured over a certain radial range. The dashed lines correspond to the mean of the total density slope in each radial range, with the same color representing the same range as the histogram.

ranges. We fix the inner radial limit to be $0.4\,R_{1/2}$ so that the inner radius for the ETG with the smallest $R_{1/2}$ is larger than the simulation softening length ($\epsilon = 0.74$ kpc below $z = 1$) to avoid fiducial core features in the density profiles. The minimum value for the inner radius $0.4\,R_{1/2}$ in our IllustrisTNG ETG sample is 1.17 kpc (0.93 kpc) at $z = 0$ ($z = 0.2$). We select four different radii as the outer radial limits, namely, $R_{1/2}$, $2\,R_{1/2}$, $3\,R_{1/2}$, and $4\,R_{1/2}$. This set of radial ranges is consistent with most of the observational samples in comparison, which usually measures the total density profile within a few times the effective radius (see Section 3.2.1 and Appendix A). The median value for $R_{1/2}$ in our IllustrisTNG ETG sample is 7.53 kpc (7.51 kpc) at $z = 0$ ($z = 0.2$).

The number count distributions of γ' measured within different radial ranges of the 514 ETGs in our IllustrisTNG sample at $z = 0$ are shown in Fig. 3. The mean $\langle\gamma'\rangle$ of each distribution is indicated by the dashed line.

As it can be seen, the mean distributions of γ' that are measured within different radial ranges are in general close to 2 and have smaller mean and scatter as the outer radius increases. The decrease in the mean is due to the increasing dominance of dark matter with increasing outer radius which leads to a shallower slope (Fig. 2), and the slight decrease in the scatter is due to the reduced Poisson noise with the increase of particle counts in larger radial ranges. A summary of the mean and scatter of γ' for the ETG sample $z = 0$ is given in Table 1.

Radial range	$\langle\gamma'\rangle$	$\sigma_{\gamma'}$
$0.4\,R_{1/2} - 1\,R_{1/2}$	2.130 ± 0.012	0.282
$0.4\,R_{1/2} - 2\,R_{1/2}$	2.050 ± 0.010	0.234
$0.4\,R_{1/2} - 3\,R_{1/2}$	2.016 ± 0.009	0.199
$0.4\,R_{1/2} - 4\,R_{1/2}$	2.003 ± 0.008	0.175

Table 1. The mean and scatter of the total power-law density slope γ' of the four radial ranges over which we measured the slope for the 514 IllustrisTNG ETGs we selected. The mean $\langle\gamma'\rangle$ is shown along with its $1\,\sigma$ error and does *not* take into account any weighting of the global galactic properties, while the scatter $\sigma_{\gamma'}$ shows the standard deviation of γ'. It is obvious that the total density slope is close to isothermal ($\gamma' \approx 2$) throughout $[R_{1/2}, 4\,R_{1/2}]$ with little evolution of the mean and scatter, although it is noticeable that the mean and the scatter become smaller with increasing outer radial range.

3.2 Correlations between the total power-law slope and other galaxy properties and their comparisons to observations

As mentioned in the introduction, the presence of isothermal density profiles has been observed to be unanimous among ETGs with little intrinsic scatter (Koopmans et al. 2006; Humphrey et al. 2006; Koopmans et al. 2009; Barnabè et al. 2009, 2011; Auger et al. 2010b; Humphrey & Buote 2010; Ruff et al. 2011; Sonnenfeld et al. 2013; Tortora et al. 2014; Serra et al. 2016; Poci et al. 2017; Bellstedt et al. 2018;

Lyskova et al. 2018). This is also true for the IllustrisTNG ETGs that we have selected as demonstrated above. The formation of such an isothermality can not be observed directly. However, studies from both observations and simulations on correlations of the total density slope with the global galactic properties could shed light on the physics during the formation and evolution process of the total density profile.

In this section, we show the correlations between γ' that is measured within $0.4\,R_{1/2}$ to $4\,R_{1/2}$ and the total stellar mass M_*, the effective radius $R_{\rm eff}$, the stellar surface density Σ_*, the central velocity dispersion $\sigma_{\rm e/2}$, the stellar orbital anisotropy parameter β, the central dark matter fraction $f_{\rm DM}$ and the in-situ-formed stellar mass ratio $f_{\rm in-situ}$ of the IllustrisTNG ETGs, along with comparisons to existing literature datasets. In the following, we first give a detailed account of the adopted comparison datasets.

3.2.1 Comparison datasets

The adopted datasets are divided into three subsets categorizing (1) local ETGs through stellar dynamic modeling, (2) higher-redshift ETGs from strong lensing surveys and (3) other numerical simulations. The first category consists of early-type galaxies from the SPIDER (La Barbera et al. 2010), ATLAS$^{\rm 3D}$ (Cappellari et al. 2011, 2013a) and SLUGGS (Brodie et al. 2014) surveys as well as from the observations of the Coma cluster (Thomas et al. 2007). In particular, Tortora et al. (2014) measured the total density slopes of SPIDER and ATLAS$^{\rm 3D}$ galaxies by fitting observed central kinematics ($\sigma_{\rm e}$) with two-component dynamical mass modeling using spherical Jeans equation. Serra et al. (2016) extended the circular velocity out to $16\,R_{\rm eff}$ with a median of $6\,R_{\rm eff}$ using HI circular velocity, the total density slopes were derived using the Jeans Anisotropy Modeling (JAM) method. Poci et al. (2017) utilized a more exhaustive dataset of ATLAS$^{\rm 3D}$ for central 2D kinematics modeling and derived total density slopes γ' and central dark matter fraction $f_{\rm DM}$ within $R_{\rm eff}$. Bellstedt et al. (2018) measured the total density slopes of the SLUGGS galaxies from $0.4\,R_{\rm eff}$ to $4\,R_{\rm eff}$ using the JAM modeling method (same as model III in Poci et al. 2017). Their comparison to EAGLE and Magneticum simulated total density slopes confirmed the consistency of the simulation data with observations. We note that for all the datasets mentioned above, the quoted stellar masses are obtained by assuming a Chabrier initial mass function (Chabrier 2003). For comparisons to this dataset, we use the IllustrisTNG ETG sample at $z = 0$.

In the second category, the adopted strong lensing surveys contain early-type lensing galaxies up to redshift $z \approx 1$. Among these, the Lenses Structure and Dynamics (LSD) Survey (Treu & Koopmans 2002; Koopmans & Treu 2003; Treu & Koopmans 2004) provided 5 ETG lenses at $z \approx 0.5 - 1.0$ with total slopes shallower than isothermal. Auger et al. (2010b) reported the effective radii, central velocity dispersions, stellar masses and central dark matter fractions of galaxies from the Sloan Lens ACS (SLACS) Survey (Bolton et al. 2006, 2008; Auger et al. 2009). The total power-law density slopes were derived by combining strong lensing and stellar kinematic measurements, as practiced in Koopmans et al. (2006). Also included are measurements from Barnabè et al. (2011), who combined strong lensing and 2D stellar kinematic modeling techniques and applied it to the SLACS ETG sample. The CFHTLS-Strong Lensing Legacy Survey (Cabanac et al. 2007; Ruff et al. 2011) (SL2S) offered a deeper and wider sky coverage compared to SLACS. The total power-law density slopes and general galaxy properties of SL2S galaxies mentioned above were derived in Sonnenfeld et al. (2013). For consistency of the comparison, we convert the stellar mass measured assuming a Salpeter IMF in Ruff et al. (2011) and Sonnenfeld et al. (2013) to a Chabrier IMF using the conversion formula $M_*^{\rm Chab} = 0.61 M_*^{\rm Salp}$ (Madau & Dickinson 2014). For comparisons to this dataset, we use the IllustrisTNG ETG sample at $z = 0.2$, which is the median redshift of the above-mentioned strong lensing dataset.

The third subset consists of other numerical simulation data from both large volume and zoom-in simulations. We include the $z = 0$ data of Magneticum, Oser and Wind simulations from Remus et al. (2017) for comparison with the IllustrisTNG ETG sample at $z = 0$. The Magneticum Pathfinder simulations (Dolag et al. to be submitted) is a set of hydrodynamic cosmological simulations evolved using the SPH (smooth particle hydrodynamics) code GADGET3 with an updated SPH formulation. It implements AGN feedback, weak kinetic feedback from galactic winds and metal line cooling (Hirschmann et al. 2014; Teklu et al. 2015). The zoom-in simulations of Oser and Wind have relatively higher resolution compared to Magneticum but exclude AGN feedback. The Oser simulation includes star formation and self-regulated SN feedback, with primordial gas cooling and without galactic winds (Oser et al. 2010, 2012). The Wind simulations include metal enrichment and strong galactic winds, producing consistent SFR and baryon conversion efficiency in low mass halos, but overestimate SFR in high mass halos in the absence of AGN feedback (Hirschmann et al. 2013, 2015).

We refer the reader to Appendix A for more details on the three comparison datasets included in this section.

3.2.2 The correlation with the total stellar mass M_*

The total stellar mass of the IllustrisTNG ETGs are taken as the sum of all the stellar particles assigned to its host subhalo by SUBFIND within a 3D aperture of 30 kpc. The stellar mass range is selected to be in the range of $10^{10.7}{\rm M}_\odot \leqslant M_* \leqslant 10^{11.9}{\rm M}_\odot$ in order to compare to observations (we also use this stellar mass cut for the correlations with other global galactic properties below). Since the outer radial range for the observed total power-law density slope γ' spans a wide range form $R_{\rm eff}$ to $16\,R_{\rm eff}$ and γ' does not vary significantly from using $2\,R_{1/2}$ to $4\,R_{1/2}$ as the outer radial range, we use the total density slope calculated within the radial range of $[0.4\,R_{1/2},\, 4\,R_{1/2}]$ for the comparisons to observations and other simulation data. We also use γ' measured within this radial range for correlations with other global galactic properties studied in this work.

The correlation of the total power-law density slope and total stellar mass is shown in Fig. 4. The IllustrisTNG ETGs are shown by the blue scattered dots. The solid blue curve gives the mean of the IllustrisTNG ETG slopes, and the blue shaded region shows the standard deviation of the slope distribution. Comparisons between the IllustrisTNG data (at two redshifts) and the three datasets, namely, stel-

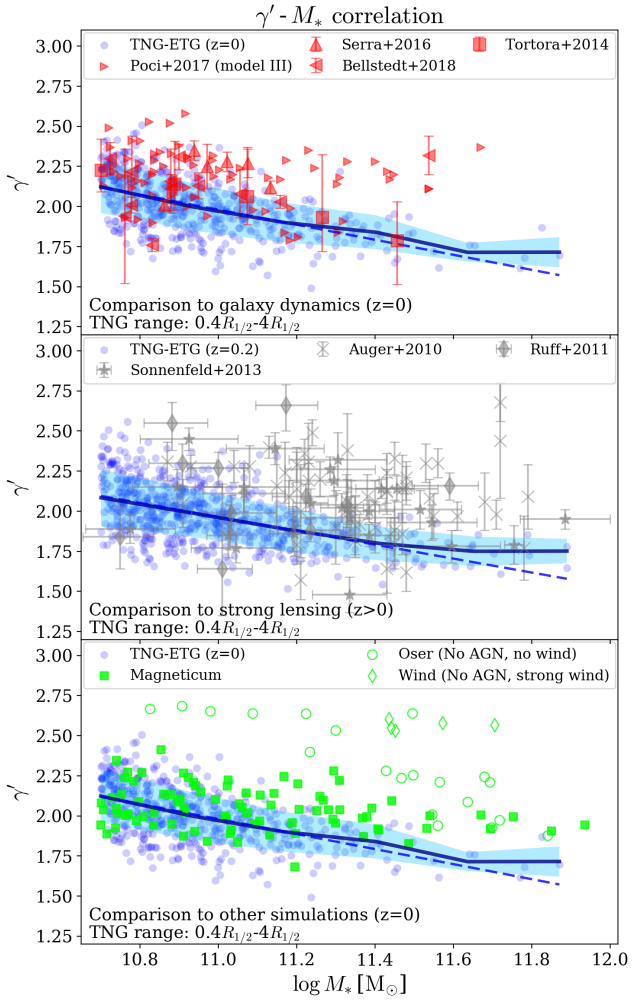

Figure 4. The correlation of the total power-law density slope γ' and the total stellar mass M_*. The IllustrisTNG ETGs are shown by the blue scattered dots. The solid blue curve gives the mean of the IllustrisTNG ETG slopes, and the blue shaded region shows the standard deviation of the slope distribution. The dashed blue line is the best linear fit to the IllustrisTNG ETG data points, with $\partial\gamma'/\partial\log M_* = -0.47 \pm 0.03$ and a Pearson correlation coefficient $r = -0.55$ for $z = 0$, and $\partial\gamma'/\partial\log M_* = -0.43 \pm 0.03$ and a Pearson correlation coefficient $r = -0.53$ for $z = 0.2$. The comparison datasets of dynamic modeling (red), strong lensing (grey) and other simulations (green) are shown in the subplots from top to bottom, respectively. The IllustrisTNG ETG slopes are calculated over the radial range $[0.4\,R_{1/2},\ 4\,R_{1/2}]$.

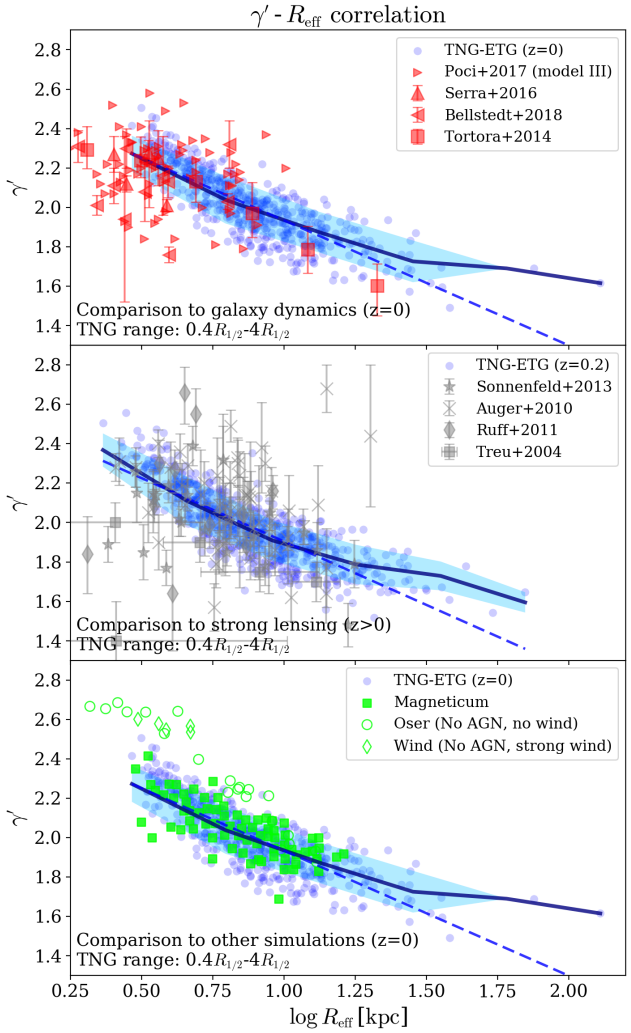

Figure 5. The correlation of the total power-law density slope γ' and the effective radius $R_{\rm eff}$. The IllustrisTNG ETGs are shown by the blue scattered dots. The effective radius that we adopt for the IllustrisTNG ETGs is approximated by their 3D stellar half mass radius $R_{1/2}$. The solid blue curve gives the mean of the IllustrisTNG ETG slopes, and the blue shaded region shows the standard deviation of the slope distribution. The dashed blue line is the best linear fit to the IllustrisTNG ETG data points, with $\partial\gamma'/\partial\log R_{\rm eff} = -0.63 \pm 0.02$ and a Pearson correlation coefficient $r = -0.82$ for $z = 0$, and $\partial\gamma'/\partial\log R_{\rm eff} = -0.64 \pm 0.02$ and a Pearson correlation coefficient $r = -0.82$ for $z = 0.2$. The comparison datasets of dynamic modeling (red), strong lensing (grey) and other simulations (green) are shown in the subplots from top to bottom, respectively. The IllustrisTNG ETG slopes are calculated over the radial range $[0.4\,R_{1/2},\ 4\,R_{1/2}]$.

lar kinematic data of local ETGs (red), strong lensing data of higher-redshift galaxies (grey) and other simulation data (green), are shown in the three subplots from top to bottom.

The dashed blue line is the best linear fit to the IllustrisTNG ETG data points, with $\partial\gamma'/\partial\log M_* = -0.47 \pm 0.03$ and a Pearson correlation coefficient $r = -0.55$ for $z = 0$, and $\partial\gamma'/\partial\log M_* = -0.43 \pm 0.03$ and a Pearson correlation coefficient $r = -0.53$ for $z = 0.2$. The power-law slope γ' decreases mildly as stellar mass M_* increases. It can be seen that the IllustrisTNG ETG data are generally in good agreement with all three datasets.

3.2.3 The correlation with the effective radius $R_{\rm eff}$

The 2D projected half light radius of the IllustrisTNG quenched galaxies has been shown to agree with observations within error bars, assuming 0.25 dex observational uncertainty in the stellar mass (Genel et al. 2018). However, different assumed stellar mass uncertainties, luminosity fitting methods, dust attenuation models, aperture shape and size, and projection effects all add up to the systematic bi-

ases in the size measurement. Therefore, we approximate the effective radius $R_{\rm eff}$ for an IllustrisTNG ETG by its 3D stellar half mass radius $R_{1/2}$ as calculated by SUBFIND, which is a model-independent size measurement intrinsic to the simulated galaxies. The correlation of the total power-law density slope and the effective radius is shown in Fig. 5. The best linear fit to the IllustrisTNG ETG data points gives $\partial\gamma'/\partial\log R_{\rm eff} = -0.63 \pm 0.02$ and a Pearson correlation coefficient $r = -0.82$ for $z = 0$, and $\partial\gamma'/\partial\log R_{\rm eff} = -0.64 \pm 0.02$ and a Pearson correlation coefficient $r = -0.82$ for $z = 0.2$. The anti-correlation between γ' and $R_{1/2}$ is more established than that of the γ'-M_* relation.

As it can be seen from Fig. 5, the IllustrisTNG ETGs produce similar trends of the $\gamma' - R_{\rm eff}$ correlation than the comparison datasets, but have systematically larger $R_{\rm eff}$, given that the stellar mass range of the comparison dataset samples is selected to match the IllustrisTNG ETG sample. Since we are approximating the effective radius of the IllustrisTNG ETGs by their 3D stellar half mass radius, this overestimation is not unexpected. Genel et al. (2018) already found that the stellar half mass radius of the IllustrisTNG quenched galaxies are larger than the observed 2D effective radius (Shen et al. 2003; Bernardi et al. 2012; van der Wel et al. 2014) by 0.3 dex (about 2 times) in the stellar mass range of $10^{10.7}{\rm M}_\odot \leqslant M_* \leqslant 10^{11.9}{\rm M}_\odot$ (their projected 2D SDSS r-band effective radius is also overestimated by 0.1–0.2 dex in the same mass range, see Fig. 2b in Genel et al. 2018). The agreement at higher redshift ($z = 0.2$) with the strong lensing dataset is marginally better than the agreement with the dynamical modeling dataset at $z = 0$, and the simulations (especially IllustrisTNG compared with Magneticum) agree better with each other than with the observational data, which could be a result of the too-strong AGN feedback model adopted in the IllustrisTNG puffing up the galaxies.

3.2.4 *The correlation with stellar surface density* Σ_*

We follow Sonnenfeld et al. (2013) and define the stellar surface density as $\Sigma_* = M_*/2\pi R_{\rm eff}^2$, where $R_{\rm eff}$ is approximated by $R_{1/2}$. The correlation of the total power-law density slope and Σ_* is shown in Fig. 6. The pronounced underestimation of the IllustrisTNG stellar surface density is a direct consequence of the 0.3 dex overestimation of $\log R_{1/2}$ of the IllustrisTNG ETGs compared to observational effective radii(Genel et al. 2018), which leads to an overall underestimation of 0.5 dex in Σ_* as shown in the figure.

The best linear fit to the IllustrisTNG ETG data points gives $\partial\gamma'/\partial\log\Sigma_* = 0.45 \pm 0.01$ and a Pearson correlation coefficient $r = 0.81$ for $z = 0$, and $\partial\gamma'/\partial\log\Sigma_* = 0.46 \pm 0.01$ and a Pearson correlation coefficient $r = 0.81$ for $z = 0.2$. The total power-law density slope increases as the stellar surface density increases. As pointed out by Auger et al. (2010b) and Dutton & Treu (2014), such a positive correlation is expected since higher stellar surface density implies a higher central baryon concentration, leading to a steeper density slope.

We note that the positive correlations in the compared observation and simulation datasets vary significantly, with Auger et al. (2010b) giving $\partial\gamma'/\partial\Sigma_* = 0.85 \pm 0.19$ for the SLACS sample, Poci et al. (2017) giving $\partial\gamma'/\partial\Sigma_* = 0.174 \pm 0.045$ for the ATLAS$^{\rm 3D}$ sample, and Remus et al. (2017) giving $\partial\gamma'/\partial\Sigma_* = 0.38$ and 0.57 for Magneticum and Oser at $z = 0$, respectively. Within the uncertainties of the comparison datasets, the IllustrisTNG $\gamma' - \Sigma_*$ correlation is in general agreement with observations and other simulations.

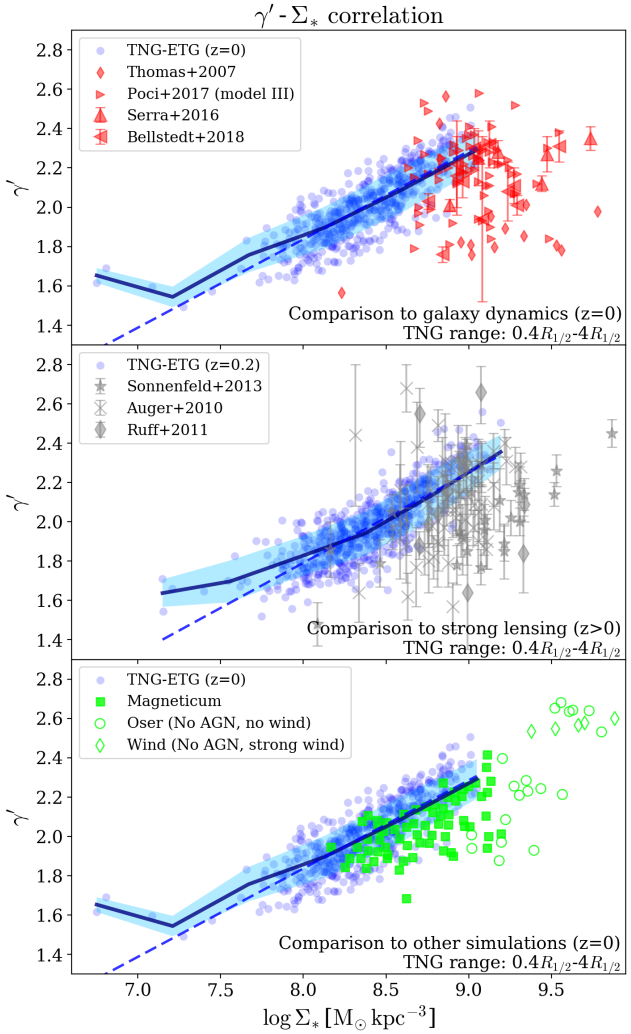

Figure 6. The correlation of the total power-law density slope γ' and the stellar surface density Σ_*. The IllustrisTNG ETGs are shown by the blue scattered dots. The solid blue curve gives the mean of the IllustrisTNG ETG slopes, and the blue shaded region shows the standard deviation of the slope distribution. The dashed blue line is the best linear fit to the IllustrisTNG ETG data points, with $\partial\gamma'/\partial\log\Sigma_* = 0.45 \pm 0.01$ and a Pearson correlation coefficient $r = 0.81$ for $z = 0$, and $\partial\gamma'/\partial\log\Sigma_* = 0.46 \pm 0.01$ and a Pearson correlation coefficient $r = 0.81$ for $z = 0.2$. The comparison datasets of dynamic modeling (red), strong lensing (grey) and other simulations (green) are shown in the subplots from top to bottom, respectively. The IllustrisTNG ETG slopes are calculated over the radial range $[0.4\,R_{1/2},\,4\,R_{1/2}]$.

3.2.5 *The correlation with stellar kinematic properties*

The central velocity dispersion $\sigma_{\rm e/2}$ is measured as the stellar-luminosity-weighted line-of-sight velocity dispersion within $0.5\,R_{1/2}$ for the IllustrisTNG ETGs. The correlation of the total power-law density slope and the central velocity

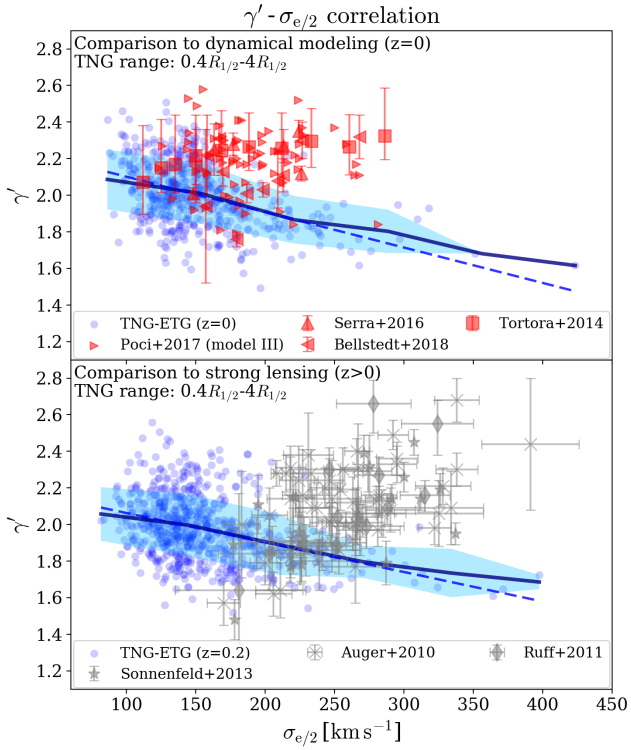

Figure 7. The correlation of the total power-law density slope γ' and the central velocity dispersion $\sigma_{e/2}$. The IllustrisTNG ETGs are shown by the blue scattered dots. The solid blue curve gives the mean of the IllustrisTNG ETG slopes, and the blue shaded region shows the standard deviation of the slope distribution. The dashed blue line is the best linear fit to the IllustrisTNG ETG data points, with $\partial\gamma'/\partial\sigma_{e/2} = -0.0019 \pm 0.0002$ and a Pearson correlation coefficient $r = -0.4343$ for $z = 0$, and $\partial\gamma'/\partial\sigma_{e/2} = -0.0016 \pm 0.0002$ and a Pearson correlation coefficient $r = -0.3726$ for $z = 0.2$. The comparison datasets of dynamic modeling (red) and strong lensing (grey) are drawn by scattered dots with error bars in the top and bottom subplots, respectively. The IllustrisTNG ETG slopes are calculated over the radial range $[0.4\,R_{1/2},\, 4\,R_{1/2}]$.

dispersion is shown in Fig. 7. The best linear fit to the IllustrisTNG ETG data points gives $\partial\gamma'/\partial\sigma_{e/2} = -0.0019 \pm 0.0002$ and a Pearson correlation coefficient $r = -0.4343$ for $z = 0$, and $\partial\gamma'/\partial\sigma_{e/2} = -0.0016 \pm 0.0002$ and a Pearson correlation coefficient $r = -0.3726$ for $z = 0.2$.

We notice that the velocity dispersions of the IllustrisTNG ETGs are systematically lower than their observational counterparts, which span a similar range in stellar masses. As it can be seen in Section 4.3 (Fig. 14), the total galaxy and halo mass (M_{200}) of the simulated galaxies are also markedly smaller than those derived for observed galaxies. Both systematic inconsistencies, combined with the excess of central dark matter fractions as found in Lovell et al. (2018), indicate potential problems with the baryonic models of the simulation, which could result in a different mix of baryons and dark matter in central regions of galaxies as well as an overestimation of baryonic sizes of galaxies.

We also point out that the strong lensing ETG sample that we compare the IllustrisTNG ETGs with also suffers from lens selection bias. The visible systematic difference in the $\sigma_{e/2}$ distribution between the two observational datasets can be explained by the fact that within the same stellar-mass range, galaxies with larger central velocity dispersion will have higher probabilities to act as gravitational lenses. Thus, strong lens galaxies in general have high stellar surface densities which leads to steeper slopes and adds an additional source of systematic bias to the total density slopes. However, quantifying the amount of systematic bias from strong lens sample selection bias is beyond the scope of this paper and will be discussed in future work.

The observed trends of the two datasets also show marked differences at $\sigma_{e/2} > 200$km/s. In fact, Auger et al. (2010b) measured $\partial\gamma'/\partial\sigma_{e/2} = 0.07 \pm 0.08$ for the SLACS sample of higher-redshift lensing galaxies, and Poci et al. (2017) obtained $\partial\gamma'/\partial\sigma_e = 0.442 \pm 0.081$ through 2D kinematics modeling for the local ETG sample.

Such differences could be rooted in the systematics of the adopted modeling methods. In particular, the total power-law density slopes for the strong-lensing sample are routinely derived under the assumption of isotropic velocity dispersion. As shown by, e.g., Koopmans et al. (2006, 2009); Xu et al. (2017), the true total density slope of a galaxy can be overestimated (underestimated) under the isotropic assumption, if its stellar kinematics is radially (tangentially) anisotropic. Also, mass-weighted slopes obtained in dynamic modeling of ETGs (e.g. Tortora et al. 2014) could also alter the γ' values. These assumptions could switch the $\gamma' - \sigma_{e/2}$ correlation from negative to positive as shown for Illustris ETGs in Xu et al. (2017) (see their Fig. 17), and this effect could account for the $\gamma' - \sigma_{e/2}$ trend discrepancy as displayed in Fig. 7.

To further investigate the possible effect from stellar anisotropy, we follow the same practice and adopt the definition of the 3D anisotropy parameter under spherical symmetry (Binney & Tremaine 2008):

$$\beta = 1 - \frac{\sigma_\phi^2 + \sigma_\theta^2}{2\sigma_r^2}, \qquad (1)$$

where σ_r, σ_ϕ and σ_θ are the velocity dispersion within the stellar half mass radius in the radial, azimuthal and polar directions, respectively. $\beta = 0$ corresponds to the isotropic case, $\beta > 0$ stands for radially biased orbits and $\beta < 0$ stands for tangentially biased orbits. In practice, we calculate β for all the stellar particles enclosed within $R_{1/2}$, each particle weighted by its stellar mass.

In Fig. 8, we show the $\gamma' - \beta$ distribution for the IllustrisTNG ETGs (solid circles) at $z = 0$, color-coded with their central velocity dispersion $\sigma_{e/2}$. Over-plotted are observational data (red triangles with error bars) from Bellstedt et al. (2018), where β came from applying the JAM modeling technique to the stellar kinematic data. The ATLAS^{3D} Survey employs an MGE (JAM) modeling method to obtain the inferred stellar mass from IFU spectroscopy (Cappellari et al. 2013b). Their model allows for non-zero stellar orbital anisotropy through adopting an anisotropy parameter $\beta = 0.25$ (Cappellari 2008) (red dotted dashed line).

The IllustrisTNG ETGs have a mean anisotropy $\langle\beta\rangle = 0.205$ (blue solid line), and a scatter of $\sigma_\beta = 0.214$ (blue dashed lines), possessing radially biased stellar orbits typical for early type galaxies, also in good agreement with observations. In addition, the most massive galaxies with higher central velocity dispersions are radially anisotropic and have

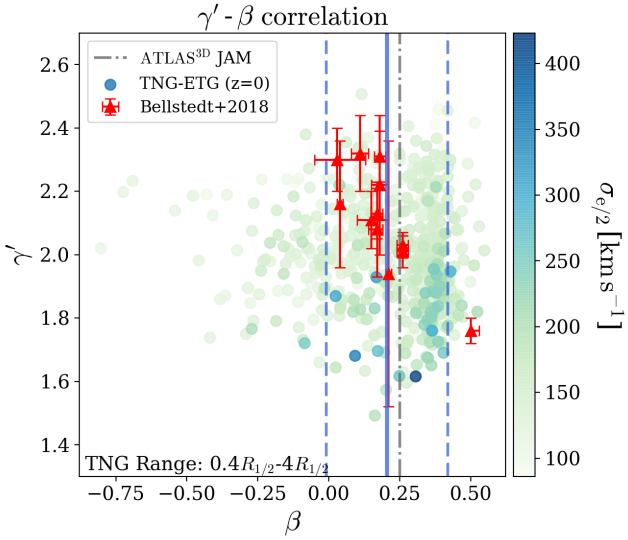

Figure 8. The correlation of the total power-law density slope γ' and the stellar orbital anisotropy parameter β. The IllustrisTNG ETGs are shown by the scattered dots, and the color index indicates the central velocity dispersion $\sigma_{e/2}$. The mean of the IllustrisTNG ETG anisotropy parameter $\langle\beta\rangle = 0.205$ is shown by the blue line, whereas the standard deviation of the β distribution $\sigma_\beta = 0.214$ is shown by the dashed lines. $\beta = 0.25$ assumed by ATLAS^{3D} (Cappellari 2008) is indicated by the grey dashed dotted line. Red triangles with error bars are JAM modeling β values from Bellstedt et al. (2018). There is no clear correlation between γ' and β for the IllustrisTNG ETGs. Also, stellar orbits are more radially (tangentially) biased in ETGs with higher (lower) central velocity dispersion.

shallower density profiles, which corresponds to giant elliptical slow rotators. The opposite corresponds to lenticular fast rotators (Li et al. 2017).

3.2.6 *The correlation with the central dark matter fraction f_{DM}*

The central dark matter fraction f_{DM} is defined as the mass ratio of dark matter over the total mass of all simulation particles enclosed within a sphere of a given radius for the IllustrisTNG ETGs. Since the stellar half mass radius of the IllustrisTNG ETGs are overestimated by a factor of 2 compared to observed effective radius values (Genel et al. 2018) , and dark matter fraction increases with the increase of radial range (Lovell et al. 2018), we measure the central dark matter fraction of the IllustrisTNG ETGs within $0.5\,R_{1/2}$, to match the adopted aperture size used in the observations (see Appendix A).

The correlation of the total power-law density slope and the central dark matter fraction is shown in Fig. 9. We note that the stellar masses of all comparison datasets have been converted to those assuming a Chabrier IMF for the consistency of the total stellar mass. A Salpeter IMF (as favored by strong lensing observations) would result in lower central dark matter fractions for observed galaxies and mitigate the apparent mismatch of f_{DM} in the middle subplot. Xu et al. (2017) found an overall overestimation of the central dark matter fraction of the Illustris ETGs when compared to the strong lensing dataset. Similar systematics have also been quantified for the IllustrisTNG simulation (Lovell et al. 2018): depending on the dataset of comparison, IllustrisTNG ETGs at $z = 0$ may have an excess of dark matter in the innermost regions of galaxies ($\lesssim R_{\rm eff}$), but consistent with available measurements at larger apertures (see Fig. 11 of Lovell et al. 2018).

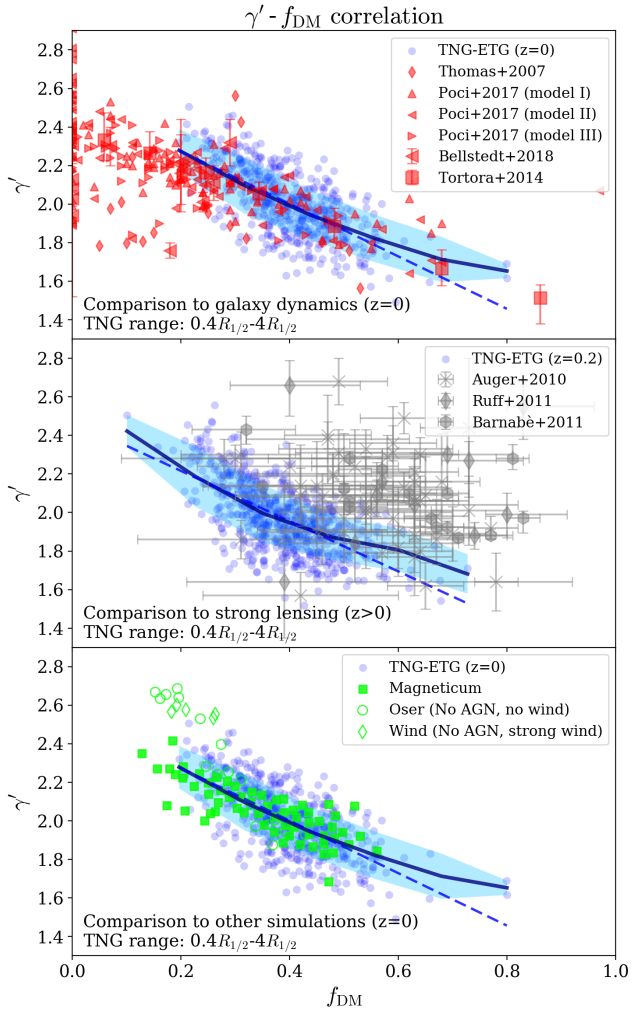

Figure 9. The correlation of the total power-law density slope γ' and the central dark matter fraction f_{DM}. For a fair comparison, we measure the central dark matter fraction of the IllustrisTNG ETGs within $0.5\,R_{1/2}$ due to the overestimation of galaxy sizes in the IllustrisTNG. The IllustrisTNG ETGs are shown by the blue scattered dots. The solid blue curve gives the mean of the IllustrisTNG ETG slopes, and the blue shaded region shows the standard deviation of the slope distribution. The dashed blue line is the best linear fit to the IllustrisTNG ETG data points, with $\partial\gamma'/\partial f_{DM} = -1.36 \pm 0.07$ and a Pearson correlation coefficient $r = -0.67$ for $z = 0$, and $\partial\gamma'/\partial f_{DM} = -1.30 \pm 0.06$ and a Pearson correlation coefficient $r = -0.64$ for $z = 0.2$. The comparison datasets of dynamic modeling (red), strong lensing (grey) and other simulations (green) are shown in the subplots from top to bottom, respectively. The IllustrisTNG ETG slopes are calculated over the radial range $[0.4\,R_{1/2},\ 4\,R_{1/2}]$.

A clear anti-correlation between γ' and f_{DM} is seen for the IllustrisTNG ETG sample. The best linear fit to the

$z = 0$ IllustrisTNG ETG dataset gives $\partial\gamma'/\partial f_{\rm DM} = -1.36 \pm 0.07$ and a Pearson correlation coefficient $r = -0.67$, in good agreement with stellar-kinematic modeling and simulation data of the Magneticum Pathfinder. The best linear fit to the $z = 0.2$ IllustrisTNG ETG dataset gives $\partial\gamma'/\partial f_{\rm DM} = -1.30 \pm 0.06$ and a Pearson correlation coefficient $r = -0.64$, in agreement with the strong lensing sample given that the sample possesses systematics of IMF inference.

3.2.7 The correlation with the in-situ-formed stellar mass ratio

We use the in-situ-formed stellar mass ratio $f_{\rm in-situ}$ as determined by the SUBLINK merger tree (Rodriguez-Gomez et al. 2015, 2016) of each galaxy in our IllustrisTNG ETG sample, and study the correlation between γ' and $f_{\rm in-situ}$. $f_{\rm in-situ}$ is defined as the stellar mass of stars formed within the main progenitor branch of the galaxy versus the total stellar mass of the galaxy at $z = 0$.

The total power-law density slope has been found to be correlated with $f_{\rm in-situ}$ (Remus et al. 2013) and anti-correlated with $f_{\rm ex-situ}$ (Dubois et al. 2013). As found in other cosmological simulations, the total density slope strongly correlates with the in-situ-formed stellar mass ratio of the galaxy. Bellstedt et al. (2018) found $\partial\gamma'/\partial f_{\rm ex-situ} = -0.44$ for Magneticum ETGs with $M_* > 10^{10.7}{\rm M}_\odot$, and for Oser ETGs Remus et al. (2017) also found a negative correlation between $f_{\rm in-situ}$ and the central dark matter fraction which indicates a positive correlation between γ' and $f_{\rm in-situ}$.

The correlation between the total power-law density slope γ' and the in-situ-formed stellar mass ratio $f_{\rm in-situ}$ for the IllustrisTNG ETGs at $z = 0$ is shown in Fig. 10. The dashed blue line is the best linear fit to the IllustrisTNG ETG data points, with $\partial\gamma'/\partial f_{\rm in-situ} = 0.56 \pm 0.03$ and a Pearson correlation coefficient $r = 0.60$. The positive correlation between $f_{\rm in-situ}$ and γ' is well produced by our IllustrisTNG ETG sample, consistent with other cosmological simulation results. Shallower (steeper) profiles correlating with lower (higher) in-situ-formed stellar mass ratios preferably in higher (lower) mass galaxies indicate the dominant role played by gas-poor dry galaxy mergers in the formation of ETGs below $z = 2$. Dry mergers occur more often for higher mass galaxies and continuously build up the density of their outskirts which lead to lower in-situ-formed stellar mass ratios and shallower total density slopes (Naab et al. 2007; Kormendy et al. 2009; Naab et al. 2009; Johansson et al. 2012; Dubois et al. 2013; Hirschmann et al. 2015).

As shown in the analysis above, the total power-law density slope of the IllustrisTNG ETGs are in broad agreement with observations considering all the correlations with galaxy parameters presented above. A summary of all the correlations with galaxy parameters for the IllustrisTNG ETGs is given in Table 2.

3.3 Galaxy redshift dependence

The redshift evolution of the total power-law density slope is shown in Fig. 11. The Illustris ETG samples at $z = [0.1, 0.2, 0.3, 0.5, 1.0, 2.0]$ are selected using the same method as we used to select the ETGs at $z = 0$ (see section 2.2 for details). The strong lensing dataset is shown by the grey scattered points with error bars along with the stellar-kinematic dataset at $z \approx 0$ shown in red in the same figure.

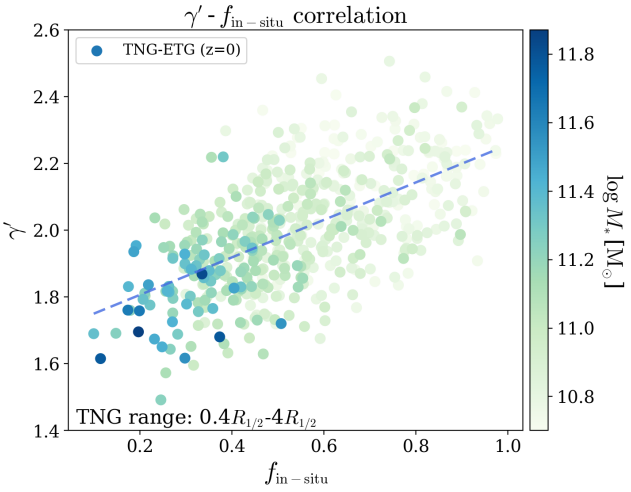

Figure 10. The correlation of the total power-law density slope γ' and the in-situ-formed stellar mass ratio $f_{\rm in-situ}$ for the IllustrisTNG ETGs at $z = 0$. The IllustrisTNG ETGs are shown by the scattered dots, and the color index indicates the total stellar mass M_*. The dashed blue line is the best linear fit to the IllustrisTNG ETG data points, with $\partial\gamma'/\partial f_{\rm in-situ} = 0.56 \pm 0.03$ and $r = 0.60$.

As it can be seen, the IllustrisTNG ETGs total density slope shows little to no evolution below $z = 1$, and displays a slight increase in the slope above $z = 1$. The best linear fit of the IllustrisTNG ETGs gives $\partial\gamma'/\partial z = 0.0227 \pm 0.0099$ and a Pearson correlation coefficient $r = 0.0375$.

As for the observational datasets, a general trend of the total density slope becoming steeper with time is demonstrated. Ruff et al. (2011) reported $\partial\gamma'/\partial z_d = -0.25^{+0.10}_{-0.12}$ for 11 SL2S lens ETGs, suggesting the that dissipative processes steepen the density profile of ETGs since $z = 1$. A similar trend was found by Sonnenfeld et al. (2013) for 36 confirmed strong lenses and 17 SL2S strong lens candidates, with $\partial\gamma'/\partial z = -0.31 \pm 0.10$, and a full redshift evolution of the total density slope $d\gamma'/dz = -0.10 \pm 0.12$ taking into account the redshift evolution of galaxy stellar mass and effective radius. Subsequent theoretical study of the evolutionary trend advocates the necessity for wet mergers involving cold gas to account for the steepening evolution of the total density profile at $z \leqslant 1$ (Sonnenfeld et al. 2014).

However, the latest cosmological simulations show tension with the currently observed redshift evolution trends. The redshift evolution trend of the Magneticum ETGs from Remus et al. (2017) with $\partial\gamma'/\partial z = 0.21$ in the redshift range $z = 0 - 2$ is displayed in Fig. 11. We neglect the Oser and Wind datasets for the γ' redshift evolution since they are zoom-in simulations with very different AGN feedback and galactic wind models, and they also have selection bias towards low density environments (Oñorbe et al. 2014). The shallowing evolutionary trend of the slope towards low redshift is significant, and large deviation from the strong lensing data is visible for $z \geqslant 0.5$. Similar trends were also discovered by Johansson et al. (2012); Remus et al. (2013); Xu et al. (2017), which favor the scenario of gas-poor dry merg-

X	$\partial\gamma'/\partial$X ($z = 0$)	r ($z = 0$)	$\partial\gamma'/\partial$X ($z = 0.2$)	r ($z = 0.2$)
$\log M_*$	-0.47 ± 0.03	-0.55	-0.43 ± 0.03	-0.53
$\log R_{\rm eff}$	-0.63 ± 0.02	-0.82	-0.64 ± 0.02	-0.82
$\log \Sigma_*$	0.45 ± 0.01	0.81	0.46 ± 0.01	0.81
$\sigma_{\rm e/2}$	-0.0019 ± 0.0002	-0.4343	-0.0016 ± 0.0002	-0.3726
$f_{\rm DM}$	-1.36 ± 0.07	-0.67	-1.30 ± 0.06	-0.64
$f_{\rm in-situ}$	0.56 ± 0.03	0.60	–	–

Table 2. The best linear fit of the correlations with galaxy parameters for our selected IllustrisTNG ETGs. X stands for the different galaxy parameters, $\partial\gamma'/\partial$X is the slope of the best linear fit correlation, and r is the Pearson correlation coefficient of the corresponding best linear fit. A '–' is assigned to any field that is not applicable.

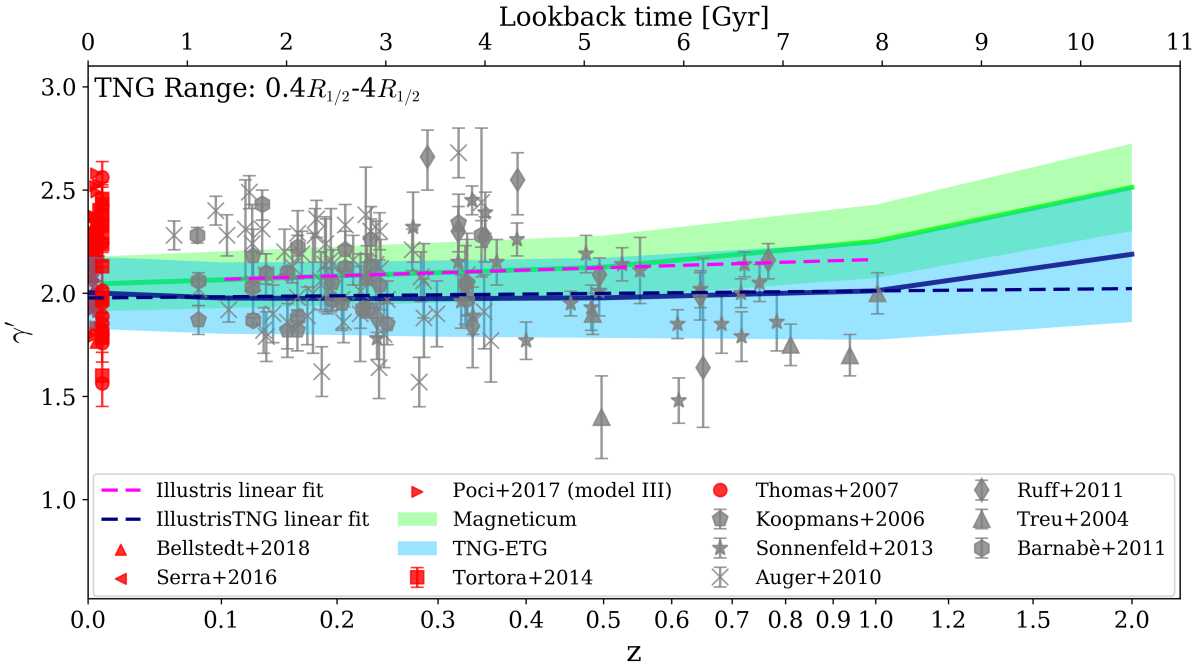

Figure 11. The evolution of the total power-law density slope with redshift. The IllustrisTNG ETG redshift evolution is shown in blue, with the solid line denoting the mean, the shaded region denoting the standard deviation, and the dashed line denoting the best linear fit. The best linear fit of the IllustrisTNG ETGs gives $\partial\gamma'/\partial z = 0.0227 \pm 0.0099$ and a Pearson correlation coefficient r = 0.0375. As for comparison, the dynamic modeling data are shown in red, and the strong lensing data are shown in grey. The Magneticum ETG redshift evolution from Remus et al. (2017) is shown in green, with the solid line denoting the mean and the shaded region denoting the standard deviation of the distribution. The best linear fit of the Illustris ETG power-law slope redshift evolution measured over the radial range $[0.5\,R_{\rm eff},\ 1.0\,R_{\rm eff}]$ is shown by the magenta dashed line (Xu et al. 2017). The IllustrisTNG ETGs show little to no evolution of the total density slope below $z = 1$, with a mild increasing trend of the slope with increasing redshift.

ers dominating the mass and size growth of ETGs at $z \leqslant 2$, leading to decreases in $f_{\rm in-situ}$ and thus shallower total density slopes with time. Interestingly, Xu et al. (2017) found a steepening trend of $\gamma_0^{\rm LD}$ towards lower redshift, where $\gamma_0^{\rm LD}$ is the slope obtained by combining strong lensing and stellar dynamics and $\partial\gamma_0^{\rm LD}/\partial z = -0.03 \pm 0.01$ with $r = -0.03$, while assuming isotropic stellar orbits for the Illustris ETGs. In contrast, a shallowing trend of the intrinsic power-law slope $\partial\gamma^{\rm PL}/\partial z = 0.11 \pm 0.01$ with $r = 0.11$ was seen for the same Illustris ETG sample. Since strong lensing slopes involve various model assumptions including isotropic stellar orbits and power-law models (Xu et al. 2016) which inevitably suffer from systematic biases, the slope redshift evolution discrepancy might be rooted in these strong model assumptions, although it is not clear if the discrepancy also involves simulation limitations. Furthermore, the strong lensing selection bias of ETGs with steeper inner slope also adds to the discrepancy.

In general, the redshift evolution of γ' of the IllustrisTNG ETGs is in line with other numerical simulations in comparison, demonstrating a decrease in the total power-law density slope with time since $z = 2$. This trend still exhibits some tension with the strong lensing observation dataset, which suggests a seemingly increasing slope with time. In our upcoming paper (Wang et al. in preparation), we will aim at quantifying the effects of galaxy mergers, star formation activities, and feedback processes on the formation and evolution of the isothermal density profile. Thereby we will also present in depth a full comparison considering the aforementioned model and selection biases.

4 THE EFFECTS OF BARYONS ON DARK MATTER

Since neither the individual density profile of dark matter nor baryonic matter is isothermal, it is of great importance to understand how baryonic effects shape the dark matter halo and how their interplay 'conspired' to form the observed near-isothermal density profiles. In this section we present comparisons of dark matter profiles made between the TNG100-full physics (FP) and the TNG100-dark matter only (DMO) runs in order to investigate the impact of baryons on dark matter. All baryonic particles (stellar, gas and BH particles) in the DMO run are converted for this purpose to collisionless dark matter particles and baryonic processes (AGN feedback, galactic winds, star formation etc.) are ignored. Dark matter halos in the DMO run are identified with their FP halo counterparts using the SUBLINK algorithm. Although not all halos in the FP run have DMO counterparts, our choice of 'central' ETGs in the FP run of TNG100 maximally mitigates this problem. However, we point out that out of the 514 DMO counterparts, only 500 are 'central' halos, and 14 are 'satellite' halos.

4.1 The power-law density slope of the dark matter component $\gamma'_{\rm DM}$

The fiducial 'stellar half mass radius' and the radial range over which we measure the power-law density slope for the DMO run halo is chosen to be identical to its corresponding FP halo. The slope distribution of the four radial ranges are shown in the four subplots of Fig. 12. In each subplot, the DMO slope distribution is shown by the black histogram, whereas the total and dark matter slopes of their FP counterparts are shown by the blue and the grey histograms, respectively. The dashed lines represent the mean of the slope distributions, with the same color legend as the solid histograms. The mean and standard deviation of the slope distributions are summarized in Table 3.

As it can be seen from the figure, the slopes of the DMO halos are generally shallower than the dark matter slope of their counterparts in the FP run within all four radial ranges investigated here. The DMO slopes also possess larger scatter than the FP slopes (see Table 3). The DMO slopes ($\langle\gamma'_{\rm DM,\,DMO}\rangle \approx 1.5$) are in good agreement with Remus et al. (2013), in which the dark matter power-law density slope is measured over the radial range $[0.3\,R_{1/2}, 4\,R_{1/2}]$, very similar to our IllustrisTNG ETG radial range. This suggests that the presence of baryons and the baryonic processes steepen both the total and the dark matter power-law density slopes simultaneously.

4.2 The inner slope of the gNFW profile

Since dark matter halos are well-modeled by the NFW profile (Navarro et al. 1997) instead of the power-law model, and in order to make fair comparisons with observations, we also fit a generalized NFW (gNFW) profile to the dark matter component in both the FP and the DMO runs with a variable inner slope Γ' (Zhao 1996):

$$\rho(r) = \rho_0 \left(\frac{r}{r_{\rm s}}\right)^{-\Gamma'} \left(1 + \frac{r}{r_{\rm s}}\right)^{-3+\Gamma'}, \qquad (2)$$

Run	Radial range	$\langle\gamma'_{\rm DM}\rangle$	$\sigma_{\gamma'_{\rm DM}}$
DMO	$0.4\,R_{1/2} - 1\,R_{1/2}$	1.344 ± 0.008	0.189
DMO	$0.4\,R_{1/2} - 2\,R_{1/2}$	1.460 ± 0.007	0.149
DMO	$0.4\,R_{1/2} - 3\,R_{1/2}$	1.516 ± 0.006	0.138
DMO	$0.4\,R_{1/2} - 4\,R_{1/2}$	1.556 ± 0.006	0.133
FP	$0.4\,R_{1/2} - 1\,R_{1/2}$	1.702 ± 0.008	0.189
FP	$0.4\,R_{1/2} - 2\,R_{1/2}$	1.723 ± 0.006	0.147
FP	$0.4\,R_{1/2} - 3\,R_{1/2}$	1.738 ± 0.005	0.124
FP	$0.4\,R_{1/2} - 4\,R_{1/2}$	1.755 ± 0.005	0.110

Table 3. The mean and standard deviation of the dark matter power-law density slope $\gamma'_{\rm DM}$ of the four radial ranges on which we measure the slope for the IllustrisTNG DMO halos and their FP counter parts. The inner radius is set to $0.4\,R_{1/2}$ and we select the different outer radii as $R_{1/2}$, $2\,R_{1/2}$, $3\,R_{1/2}$, and $4\,R_{1/2}$ following Section 3.1. The 'Run' column corresponds to the dark matter only (DMO) run and the full physics (FP) run, respectively.

Run	$\langle\Gamma'\rangle$	$\sigma_{\Gamma'}$
DMO	1.350 ± 0.009	0.192
FP	1.607 ± 0.008	0.178

Table 4. The mean and the standard deviation of the inner slope Γ' of the best fit gNFW profile to the DMO halos and the dark matter component in their FP counterparts. The 'Run' column indicates the type of the simulation: the dark matter only (DMO) run and full physics (FP) run. The mean $\langle\Gamma'\rangle$ is shown along with its $1\,\sigma$ error and does *not* take into account any weighting of the global galactic properties, while the scatter $\sigma_{\Gamma'}$ shows the standard deviation of the distribution.

where ρ_0 is the characteristic density and $r_{\rm s}$ is the scale radius. We fit (with equal radial weighting) the gNFW profile only to the 545 'central' halos in the DMO run and their corresponding FP ETGs within $[0.01\,R_{200}, R_{200}]$ of each halo (ETG). The distribution of the inner slope Γ' compared with the power-law density slope of the dark matter component $\gamma'_{\rm DM}$ over the radial range $[0.4\,R_{1/2}, 4\,R_{1/2}]$ is shown in Fig. 13. The mean and the standard deviation of the inner slope are summarized in Table 4.

It can be seen from Fig. 13 that Γ' in both the FP and the DMO runs is shallower than the dark matter power-law slope $\gamma'_{\rm DM}$ measured within the investigated radial ranges in the corresponding run. The more important aspect of the slope distribution is that the inner slopes Γ' of the TNG FP ETGs are much steeper than their DMO counterparts, whose Γ' are closer to the standard NFW inner slope $\Gamma' = 1$. The steepening reflects dark matter halo contraction due to the presence of baryons and dissipation processes.

4.3 The correlation of the inner slope Γ' with the halo mass M_{200}

The correlation of the gNFW inner slope Γ' and the halo mass M_{200} is shown in Fig. 14. The IllustrisTNG FP ETGs are shown by the blue scattered dots in the upper panel, and their corresponding DMO halos are shown by the red scattered dots in the lower panel. The solid curve in each panel shows the mean of the inner slopes, and the shaded region shows the standard deviation of the inner slope distribution.

The dashed line in each subplot is the best linear fit to the $\Gamma' - M_{200}$ correlation, with $\partial\Gamma'_{\rm FP}/\partial\log M_{200} = -0.1828 \pm 0.0204$ and a Pearson correlation coefficient $r = -0.3719$ for

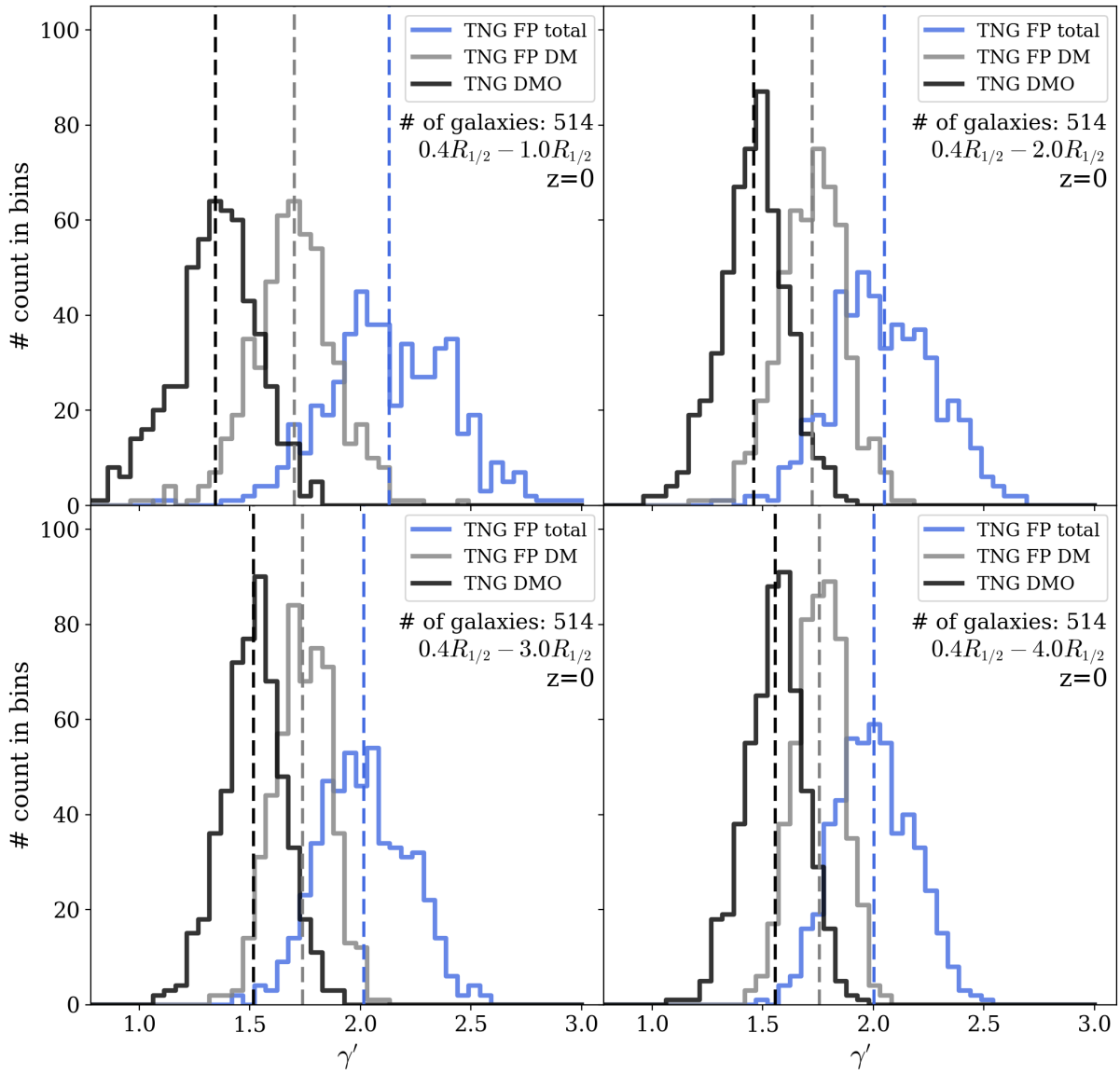

Figure 12. Comparison between the power-law density slopes in the IllustrisTNG DMO (dark matter only) and the IllustrisTNG FP (full physics) ETGs at $z = 0$. The slope distribution of the four radial ranges are shown in the four subplots. In each subplot, the DMO slope distribution is shown by the black histogram, whereas the total and dark matter slopes of their FP counterparts are shown by the blue and the grey histograms, respectively. The dashed lines represent the mean of the slope distributions and with the same color legend as the solid histograms. The slopes of the DMO halos ($\langle\gamma'_{\rm DM,\,DMO}\rangle \approx 1.5$, in agreement with Remus et al. 2013) are shallower than the dark matter component in their FP counterparts ($\langle\gamma'_{\rm DM,\,DMO}\rangle \approx 1.7$) within all four radial ranges investigated here.

the FP dark matter components, and $\partial\Gamma'_{\rm DMO}/\partial{\rm log}M_{200} = 0.0044 \pm 0.0237$ with a Pearson correlation coefficient $r = 0.0082$ for the DMO dark matter halos. We use the halo mass of the FP counterparts of the DMO halos for consistency. While the inner slopes $\Gamma'_{\rm DMO}$ of the DMO halos is almost constant with halo mass, $\Gamma'_{\rm FP}$ of the FP halos steepens as the halo mass M_{200} decreases, indicating that the presence of baryons and baryonic processes is essential to steepen the inner slope of the dark matter halo, especially in lower-mass galaxies, and for forming the observed negative trend of the $\Gamma' - M_{200}$ correlation. This is also consistent with the fact that lower-mass ETGs also possess a higher (lower) central baryonic (dark matter) fraction (also see Fig. 11 in Xu et al. (2017) and Fig. 9 in Lovell et al. 2018).

We compare the IllustrisTNG $\Gamma' - M_{200}$ correlation with the observed and simulated results. Over-plotted in Fig. 14 are measurements for observed and simulated galaxies plotted with error bars. Newman et al. (2015) modeled 10 group scale lenses and inferred the dark matter power-law density slope $\gamma'_{\rm DM}$ within the effective radius combining dynamical constraints. Sonnenfeld et al. (2015) selected 81 strong lenses from the SL2S and SLACS surveys and modeled their inner slope Γ' of the dark matter profile using joint lensing and stellar dynamics method. Oldham & Auger (2018) modeled 12 strong lenses combined with stellar kinematics to determine the inner slope. Wasserman et al. (2018) modeled a single ETG NGC1407 using Jeans modeling with varying radial IMF and kinematic tracers to constrain the dark mat-

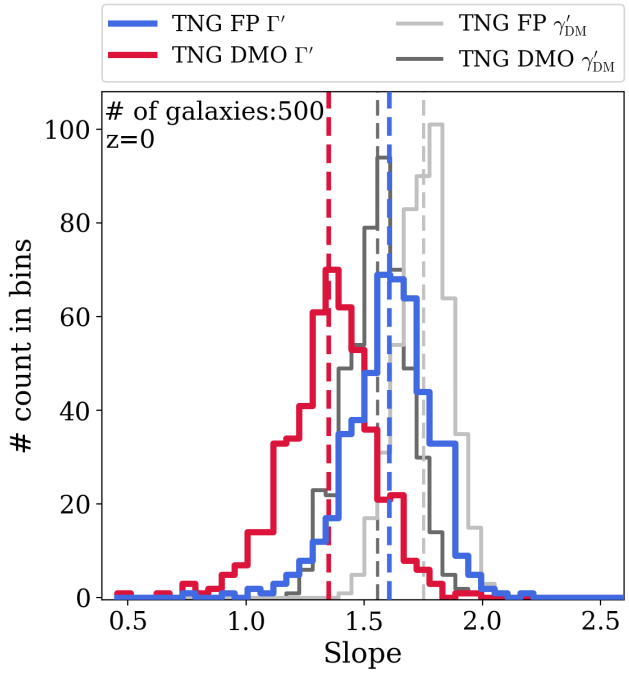

Figure 13. Comparison between the gNFW inner slope Γ' and the dark matter power-law density slope $\gamma'_{\rm DM}$ in the DMO and the FP runs at $z = 0$. Shown here are only the 545 'central' halos in the DMO run along with their FP counterparts. $\gamma'_{\rm DM}$ is measured over the radial range $[0.4\,R_{1/2},\ 4\,R_{1/2}]$. The inner slopes of the gNFW profile in the FP and the DMO runs are shown by the blue and the red histograms, while the dark matter power-law density slopes in the FP and the DMO runs are given by the light and dark grey histograms. The dashed lines represent the mean of the distributions, with the same color legend as the solid histograms.

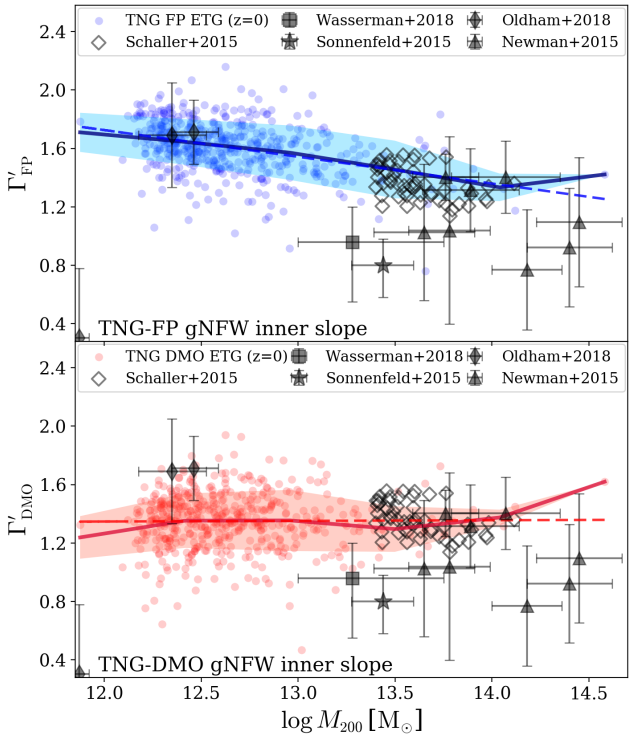

Figure 14. The correlation of the gNFW inner slope Γ' with the halo mass M_{200} in the FP ETGs versus their halo mass at $z = 0$. The IllustrisTNG FP ETGs are shown by the blue scattered dots in the upper panel, and their corresponding DMO halos are shown by the red scattered dots in the lower panel. The solid curves in each panel give the mean of the inner slopes, and the shaded regions show the standard deviations of the inner slope distribution. The dashed lines are the best fits to the $\Gamma' - M_{200}$ correlation, with $\partial\Gamma'_{\rm FP}/\partial\log M_{200} = -0.1828 \pm 0.0204$ and a Pearson correlation coefficient $r = -0.3719$ for the FP dark matter components, and $\partial\Gamma'_{\rm DMO}/\partial\log M_{200} = 0.0044 \pm 0.0237$ with a Pearson correlation coefficient $r = 0.0082$ for the DMO dark matter halos. The comparison datasets are shown in black and are identical in the two panels. Note that the halo mass used for the DMO halos is the M_{200} of their FP counterparts, for consistency.

ter inner slope. As for the simulated values, Schaller et al. (2015b) selected halos from the EAGLE simulation (Schaye et al. 2015) and modeled the inner slope Γ' of their dark matter halos. We only include their small-mass halos which are similar in mass to our selected IllustrisTNG ETGs. We refer the reader to Appendix B for more details on the comparison dataset included in this section.

Comparison between the IllustrisTNG FP data (upper panel) and the datasets from observations and other simulation reveals that the correlation of the inner slope with the halo mass is in good agreement with the observed and simulated values. Intriguingly, the IllustrisTNG FP data bridges the gap between the galaxy-size halos ($\lesssim 10^{12}\mathrm{M}_\odot$) and group-size halos ($\gtrsim 10^{14}\mathrm{M}_\odot$), which indicates a tight $\Gamma' - M_{200}$ correlation, and we expect newly observed samples within this halo mass range to possess inner slopes similar to the IllustrisTNG values.

We note that the total power-law density slope γ' of the IllustrisTNG ETGs is positively correlated with the FP dark matter inner slope $\Gamma'_{\rm FP}$ at $z = 0$ as shown in Fig. 15. The scattered dots denoting the IllustrisTNG ETGs are colored by the halo mass M_{200} of each galaxy. The best linear fit of the $\Gamma'_{\rm FP} - \gamma'$ correlation gives $\partial\Gamma'_{\rm FP}/\partial\gamma' = 0.77 \pm 0.03$ and a Pearson correlation coefficient $r = 0.76$. The total density slope γ' is also anti-correlated with the halo mass M_{200} as seen from the figure. The halo mass of the simulated galaxies are significantly smaller than those derived for observed galaxies, which points to an overestimation of baryonic sizes of galaxies, consistent with the excess of central dark matter fractions as found in Lovell et al. (2018).

We also note that some previous studies which built the dynamic model through the Jeans equations set priors on the dark matter inner slope Γ' from 0 to 1.6 (e.g. Li et al. 2017), or even smaller (0 to 1.2, Cappellari et al. 2013b). Our analysis above suggests that this prior is better broadened to [0, 2].

A summary of the $\Gamma' - M_{200}$ correlations presented in this section for the IllustrisTNG ETGs is given in Table 5.

4.4 The correlation of the inner slope Γ' with the halo concentration c_{200}

We show the correlation of the inner slope Γ' with the halo concentration c_{200} at $z = 0$ in Fig. 16. The upper and bot-

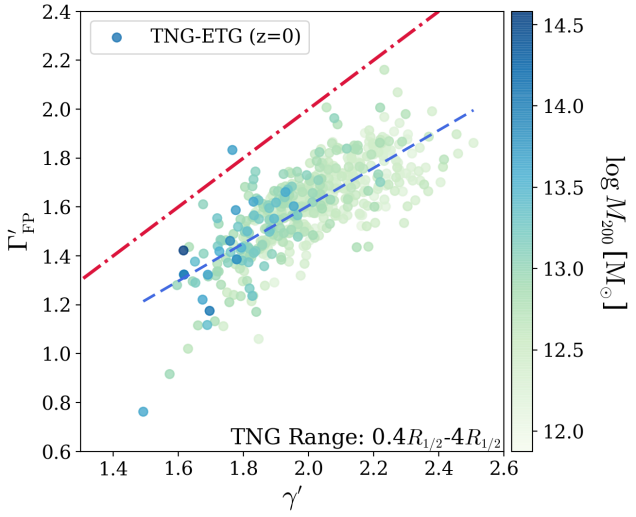

Figure 15. The correlation of the gNFW inner slope $\Gamma'_{\rm FP}$ with the total power-law density slope γ'. The scattered dots denoting the IllustrisTNG ETGs are colored by the halo mass M_{200} of each galaxy. The red dotted dashed line is the line where $\Gamma'_{\rm FP} = \gamma'$. The blue dashed line is the best linear fit to the correlation, with $\partial\Gamma'_{\rm FP}/\partial\gamma' = 0.77 \pm 0.03$ and a Pearson correlation coefficient $r = 0.76$. The total density slope γ' is also anti-correlated with the halo mass M_{200} as seen from the figure.

Run	$\partial\Gamma'/\partial\log M_{200}$	r
FP	-0.1828 ± 0.0204	-0.3719
DMO	0.0044 ± 0.0237	0.0082

Table 5. The best linear fit of the $\Gamma' - M_{200}$ correlations presented in Section 4.3. 'Run' stands for the different galaxy parameters, $\partial\Gamma'/\partial\log M_{200}$ is the slope of the best linear fit to the correlation, and r is the Pearson correlation coefficient of the corresponding best linear fit. All values are given for $z = 0$.

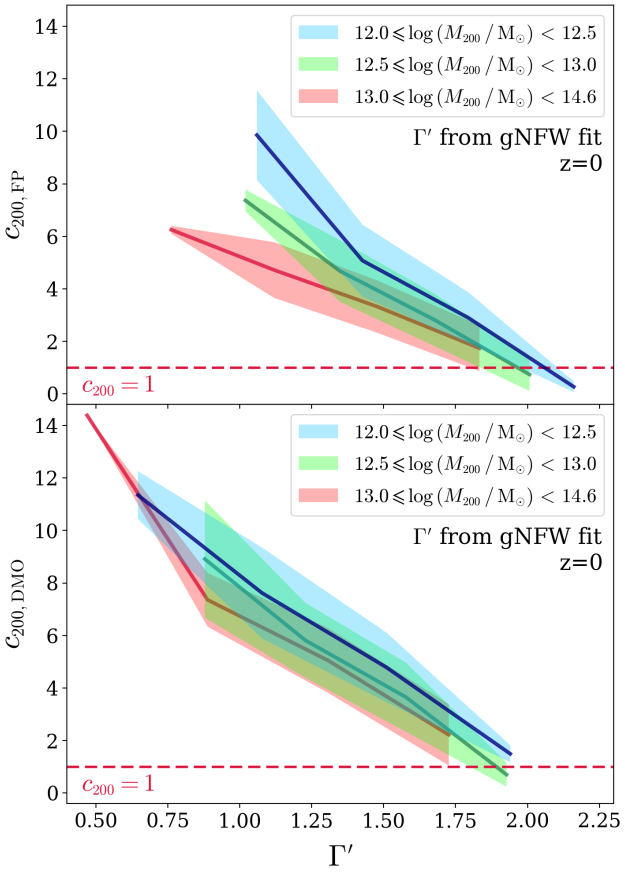

Figure 16. The correlation of the inner slope Γ' with the halo concentration c_{200} in the FP run (upper panel) and DMO run (lower panel) at $z = 0$. The halos are divided into three mass bins, labeled in blue, green and red as indicated in the legend box, containing 218, 212 and 70 ETGs, respectively. The solid lines represent the mean while the shaded regions represent the standard deviation of the distribution. It is seen from the figure that c_{200} decreases with increasing inner slope Γ' in both the FP and the DMO run. The red dashed line in each subplot indicates where $c_{200} = 1$ and exposes extreme outliers with $c_{200} < 1$ at the large Γ' end in both the FP and DMO run. These halos have concentrations with $c_{200} > 1$ if we perform a standard NFW fit. Note that the halo mass used for the DMO halos is the M_{200} of their FP counterparts, for consistency.

tom panels represent the FP and the DMO cases, respectively. The halos are divided into three mass (FP halo mass M_{200}) bins, namely $12.0 \leqslant \log(M_{200}/M_\odot) < 12.5$, $12.5 \leqslant \log(M_{200}/M_\odot) < 13.0$, $13.0 \leqslant \log(M_{200}/M_\odot) < 14.6$, containing 218, 212 and 70 ETGs, respectively. We use the halo mass of the FP counterparts for the DMO halos for consistency.

It is seen from the figure that c_{200} decreases with increasing inner slope Γ' in both the FP and the DMO run, regardless of halo mass range. Also, there are a few extreme outliers with $c_{200} < 1$ in both the FP and the DMO run. These halos have concentrations with $c_{200} > 1$ if we perform a standard NFW fit ($c_{200,\rm FP} > 3.48$ and $c_{200,\rm DMO} > 4.40$). Hence, this issue is mainly caused by our choice of the gNFW profile model. Furthermore, the concentration parameter c_{200} decreases with increasing halo mass range. This is consistent with the $c_{200} - M_{200}$ correlation compared to observations and other simulations (Macciò et al. 2007; Neto et al. 2007; Duffy et al. 2008; Gao et al. 2008; Dutton & Macciò 2014; Schaller et al. 2015a), and it will be elucidated in more detail in an upcoming IllustrisTNG paper (Pillepich et al. in preparation).

The fact that the dark matter inner slope decreases with increasing c_{200} is more significant for the lower-mass systems. For a standard NFW profile, a higher c_{200} indicates a smaller scale radius and higher concentration. However, larger Γ' also indicates a cuspy dark matter core and probable halo contraction. This suggests that when dark matter halos are highly concentrated, the standard NFW c_{200} might not provide an objective measure of the halo concentration, and one must combine the values of c_{200} and Γ' of a gNFW profile to determine the concentration of dark matter halos. This is also in line with the suggestion of modeling steeper dark matter profiles in observations proposed in Lovell et al. (2018).

As an illustration of this issue, we show three halos from the FP run (upper panels) that have similar R_{200} (M_{200}) but dramatically different c_{200} along with their DMO counter-

parts (lower panels) in Fig. 17. In the upper (lower) panels, the blue (red) scattered dots represent the measured 3D dark matter radial density, and the blue (red) dashed curve is the best gNFW fit to the dark matter radial density profile. The upper left panel shows a halo with dark matter inner slope close to the standard NFW inner slope ($\Gamma' \approx 1$), the upper middle panel shows a halo with inner slope steeper than the NFW inner slope ($\Gamma' \approx 1.7$), and the upper right panel shows an extremely steep inner slope case ($\Gamma' \approx 2$). Their DMO counterparts in the lower panels have shallower gNFW inner slopes. Since the gNFW profile enforces a constant outer slope of 3, larger inner slopes correspond to larger scale radii r_s and hence lower concentration parameters c_{200}, which is present in both the FP and the DMO cases. It is not clear, however, why halos of similar masses can have markedly different concentrations (i.e. the large range of c_{200} in Fig. 16). Environment and merger histories might play important roles, although we leave this issue to future work to address.

4.5 The correlation of the mass-weighted slope $\gamma'_{\rm mw}$ with central dark matter fraction $f_{\rm DM}$

The steeper dark matter inner slopes of IllustrisTNG-FP ETGs compared with their DMO counterparts (Fig. 13 and Fig. 14) and the anti-correlation of $c_{200} - \Gamma'$ (Fig. 16 and Fig. 17) are essentially in agreement with the predictions of dark matter halo contraction.

Adiabatic halo contraction originally proposed that the dissipative infall of gas contracts dark matter and creates dense cores in the center of halos (Blumenthal et al. 1986). However, subsequent studies of gas cooling in hydrodynamical simulations favored less contraction than the prediction of the adiabatic contraction scheme, but still found halos to be contracted and the dark matter profiles in the inner region to be steeper than the standard NFW profile (Gnedin et al. 2004; Abadi et al. 2010). These findings are also self-consistent in predicting the transformation of prolate halos to oblate ones through dissipation which matches the shape distribution of the observed early-type galaxies (Dubinski 1994; Abadi et al. 2010).

Nevertheless, subsequent observations exposed tension about the level of contraction of dark matter halos. Sonnenfeld et al. (2012) measured the dark matter slope of SDSSJ0946+1006 giving $\gamma'_{\rm DM} = 1.7 \pm 0.2$, suggesting strong contraction in concordance with simulations (Duffy et al. 2010). Grillo (2012) measured average dark matter slopes for SLACS lenses of $\langle\gamma'_{\rm DM}\rangle = 1.7 \pm 0.5$, which was later corrected by Dutton & Treu (2014) to $1.40^{+0.15}_{-0.26}$ assuming a Salpeter IMF, favoring mild contraction. Similarly, Newman et al. (2015) obtained $\langle\gamma'_{\rm DM}\rangle = 1.35 \pm 0.09$ for 10 group-scale lenses, with mild contraction in agreement with Gnedin et al. (2004). Interestingly, Oguri et al. (2014) found the best-fit dark matter slope for 85 SLACS strong lenses (Auger et al. 2009) to be $\gamma'_{\rm DM} = 1.60^{+0.13}_{-0.18}$, steeper than Newman et al. (2015) but favoring the standard NFW profile without contraction combined with the radial distribution of dark matter fraction. Hydrodynamical simulations (Oser et al. 2012; Remus et al. 2013) favor dark matter component slopes $\gamma'_{\rm DM} \leqslant 1.5$ for ETGs, implying little to no contraction in the dark matter halo. Thus, the dark matter slope does not directly indicate the level of contraction, and one must also account for the central dark matter fraction to constrain the level of contraction.

To further quantify the level of contraction of the IllustrisTNG ETG dark matter halos, we compare the correlation of the mass weighted slope $\gamma'_{\rm mw}$ and the central dark matter fraction $f_{\rm DM}$ with the semi-empirical models presented in Shankar et al. (2017). Utilizing a 'Sérsic-NFW' model and comparing their predictions with observational data (Newman et al. 2013; Sonnenfeld et al. 2015), they have ruled out at $\gtrsim 2-3\,\sigma$ deviations from a Sérsic stellar profile and an uncontracted NFW dark matter profile. The $\gamma'_{\rm mw}-f_{\rm DM}$ correlation predicted by their standard NFW model, contracted NFW model and expanded NFW model are shown along with our IllustrisTNG ETG sample and binned values of the $\gamma'_{\rm mw} - f_{\rm DM}$ correlation from SPIDER and ATLAS$^{\rm 3D}$ (Tortora et al. 2014) in Fig. 18. The slopes from the Shankar et al. (2017) models and Tortora et al. (2014) are the mass-weighted density slopes (Dutton & Treu 2014) measured at the effective radius of each galaxy. The contraction and expansion levels of the semi-analytical models are less extreme than the adiabatic case (Shankar et al. 2017).

As shown in Fig. 18, the semi-empirical model with standard NFW profile, with halo contraction, and with halo expansion are shown by the orange, blue and green dashed curves, respectively. The binned values of SPIDER and ATLAS$^{\rm 3D}$ (Tortora et al. 2014) data are shown by the red squares with error bars (same as Fig. 9). The mass weighted slope at the effective radius ($R_{1/2}$) versus the central dark matter fraction of the IllustrisTNG ETGs are shown by the colored scattered dots, with the color index indicating the total stellar mass. The navy curve and the shaded blue region are the mean and the standard deviation of the IllustrisTNG ETG slope distribution. It is obvious that the mean of the IllustrisTNG ETG $\gamma'_{\rm mw} - f_{\rm DM}$ correlation is in better agreement with the contracted NFW model, which corroborates the steeper dark matter slopes in the IllustrisTNG ETGs aforementioned. It is also visible that the IllustrisTNG ETGs with larger stellar mass are less contracted and get closer to the standard NFW model as well as the observation data of SPIDER and ATLAS$^{\rm 3D}$. The low mass end of our sample tends to have a steeper mass-weighted slope than the contracted NFW model, indicating a near-adiabatic contraction level. Also, a small number of halos are expanded in comparison with the models, which might share a common origin with the overestimation of $R_{1/2}$ in the IllustrisTNG ETGs. Thus, the contraction level of the IllustrisTNG ETG dark matter halos is mass dependent. Given that the central dark matter fraction ($\lesssim R_{\rm eff}$) increases with increasing stellar/halo mass in our sample mass range (Lovell et al. 2018), we conclude that baryonic processes play a more (less) significant role in the lower (higher) mass IllustrisTNG ETGs, where there is a lower (higher) central dark matter fraction.

5 CONCLUSIONS AND DISCUSSION

In this work we studied the statistical properties and the correlations of the density profiles with a number of galaxy properties of early-type galaxies (ETGs) selected from the IllustrisTNG simulations (Marinacci et al. 2018; Naiman et al. 2018; Nelson et al. 2018; Pillepich et al. 2018b; Springel et al.

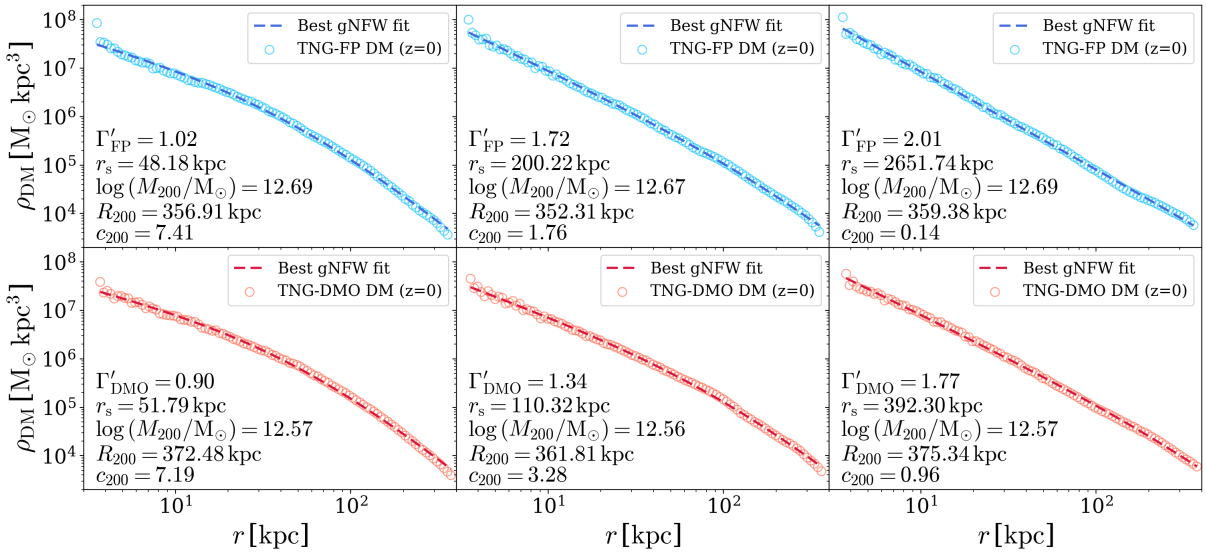

Figure 17. Three dark matter halo profiles from the FP run (upper panels) with similar R_{200} (M_{200}) which have dramatically different c_{200} as an illustration of the $c_{200}-\Gamma'$ anti-correlation. Their DMO counterparts are shown in the lower panels. In the upper (lower) panels, the blue (red) scattered dots represent the measured 3D dark matter radial density, and the blue (red) dashed curve is the best gNFW fit to the dark matter radial density profile. The upper left panel shows a halo with dark matter inner slope close to the standard NFW inner slope ($\Gamma' \approx 1$), the upper middle panel shows a halo with inner slope steeper than the NFW inner slope ($\Gamma' \approx 1.7$), and the upper right panel displays a case with an extremely steep inner slope ($\Gamma' \approx 2$). Their DMO counterparts in the lower panels have shallower gNFW inner slopes. It is obvious that increasing inner slope leads to larger best-fit scale radius $r_{\rm s}$ and hence lower c_{200}, indicating stronger halo contraction.

2018). In particular, our selection strategy which employed single and double component luminosity profile fitting of the rest frame SDSS r-band radial luminosity distribution of galaxies in the TNG100 run resulted in a sample of 514 (673) well-resolved 'central' ETGs in the stellar mass range of $10^{10.7}{\rm M}_\odot \leqslant M_* \leqslant 10^{11.9}{\rm M}_\odot$ at $z = 0$ ($z = 0.2$). We measured the total power-law density slopes of all the IllustrisTNG ETGs within four different radial ranges, and demonstrated the correlations of the total density slope with other global galactic properties including stellar mass, effective radius, stellar surface density, stellar kinematics, central dark matter fraction and in-situ-formed stellar mass ratio. Also presented is the redshift evolution of the total power-law density slopes. All of these have been compared with diverse datasets from local ETGs through stellar kinematic modeling, higher-redshift ETGs from strong lensing surveys and other numerical simulations. We also compared the dark matter density slopes of our selected ETGs in the full physics (FP) run of TNG100 with the dark matter slopes of their corresponding halos in the dark matter only (DMO) run in order to study the effects of baryons on dark matter and how they shape the total density profile. The major findings of our analysis are summarized as follows:

- We calculated the total power-law density slope of each selected IllustrisTNG ETG by performing a linear fit to the radial distribution of the 3D density in logarithmic scale within four radial ranges, with the inner radius set to $0.4\,R_{1/2}$ ($R_{1/2}$ stands for the stellar half mass radius), and the outer radius set to $R_{1/2}$, $2\,R_{1/2}$, $3\,R_{1/2}$, and $4\,R_{1/2}$. The total density slopes were found to be close to (slightly steeper than) isothermal across these radial ranges, and the intrinsic scatter of the total power-law density slope mildly decreased with increasing outer radial range (see Fig. 3 and Table 1).

- The total power-law density slope (measured over $0.4\,R_{1/2}$–$4\,R_{1/2}$ for all correlations) of the IllustrisTNG ETGs shows a mild anti-correlation with their total stellar mass, an anti-correlation with their effective radius (approximated by $R_{1/2}$), and a positive correlation with their stellar surface density. These trends are in broad agreement with observations and other simulations (see Fig. 4, Fig. 5 and Fig. 6), except that the stellar half mass radius of the IllustrisTNG ETGs are larger by 1.5-2 times compared to the effective radius from observations (Genel et al. 2018), which leads to about 2 times smaller values of the stellar surface density compared to observational data in the same stellar mass range.

- The total power-law density slope of the IllustrisTNG ETGs shows a mild anti-correlation with their central velocity dispersion, in tension with the observational datasets (see Fig. 7). Nevertheless, the slopes derived for the observational sample may suffer from systematic biases under the isotropic velocity dispersion assumption, such that the more-massive galaxies which are radially anisotropic tend to have overestimated total density slopes (see Fig. 8 and also Fig. 17 of Xu et al. 2017). The apparent underestimation of $\sigma_{\rm e/2}$ in comparison with observations suggests limitations in baryon models.

- The total power-law density slope of the IllustrisTNG ETGs exhibits an anti-correlation with the central dark matter fraction, and the trend marginally agrees with the comparison datasets at $z = 0$ (see Fig. 9). The agreement with the strong lensing dataset at $z > 0$ would be better had we chosen a Salpeter IMF instead of a Chabrier IMF (chosen for stellar mass consistency), due to the $f_{\rm DM} - {\rm IMF}$ degeneracy.

- The power-law density slope of the IllustrisTNG ETGs also shows a clear positive correlation with the in-

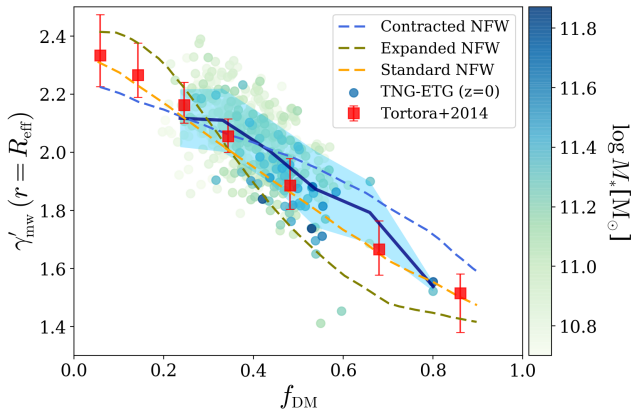

Figure 18. The $\gamma'_{\rm mw} - f_{\rm DM}$ correlation in comparison with semi-empirical models (Shankar et al. 2017) and observations (Tortora et al. 2014). The mass-weighted slope is measured at the effective radius. The semi-empirical models with standard NFW profile, with halo contraction, and with halo expansion are shown by orange, blue and green dashed curves, respectively. The binned values of SPIDER and ATLAS^{3D} (Tortora et al. 2014) data are shown by the red squares with error bars (same as Fig. 9). The mass weighted slopes at the effective radius ($R_{1/2}$) versus the central dark matter fraction of the IllustrisTNG ETGs are shown by the colored scattered dots, with the color bar indicating the total stellar mass. The navy curve and the shaded blue region are the mean and the standard deviation of the IllustrisTNG ETG slope distribution.

situ-formed stellar mass ratio, which indicates that gas-poor galaxy mergers may have played a dominant role in evolving the total density profile shallower with time. Such an effect is more significant in higher-mass ETGs compared to their lower-mass counterparts (see Fig. 10).

• The total power-law density slope is nearly independent of redshift below $z = 1$, mildly decreasing with time. The trend shows some tension with the observed slope redshift dependence (see Fig. 11).

• We calculated the slopes of the dark matter component of the IllustrisTNG ETGs and their corresponding dark matter only counterparts over the same radial ranges used for the measurements of their total slopes. The slopes of the dark matter only halos were in general shallower than their full physics counterparts and possessed larger intrinsic scatter in comparison (see Fig. 12 and Table 3). The inner slopes of the best fit gNFW profile were shallower than the total power-law density slopes, and the FP inner slopes were much steeper than the standard NFW profile, indicative of halo contraction.

• The dark matter profile inner slope is anti-correlated with the halo mass in the FP run, and shows almost no correlation with the halo mass in the DMO run. The trends were in good agreement with the observed and simulated datasets (see Fig. 14). The total density slope γ' is positively correlated with the FP inner slope $\Gamma'_{\rm FP}$ and anti-correlated with the halo mass (see Fig. 15). We suggest that the prior of the dark matter profile inner slope should be broadened to [0, 2] in dynamic modeling studies.

• The dark matter inner slope is anti-correlated with the halo concentration parameter (see Fig. 16), indicating non-universal representation of dark matter halos by the gNFW profile, possibly due to different environment and merger history issues (see Fig. 17 for an illustration). Comparison of the $\gamma'_{\rm mw} - f_{\rm DM}$ with semi-analytical models and observations revealed that the dark matter halos of the IllustrisTNG ETGs are indeed contracted. The IllustrisTNG ETGs with smaller stellar mass and central dark matter fraction have more significant contraction, while the ETGs with larger stellar mass and central dark matter fraction show little to no contraction (see Fig. 18). The halo contraction level of the IllustrisTNG ETGs is mass dependent and is consistent with the indications of the IllustrisTNG galaxy dark matter fractions presented in (Lovell et al. 2018).

Overall, our selected sample of IllustrisTNG ETGs reproduced remarkably well the observed statistical property of near-isothermal density profiles with little intrinsic scatter. The sample also demonstrated its fidelity through the broad agreement of the correlations between the total density slope and the global galactic properties in comparison with observations and other simulations. Since the IllustrisTNG model was not intentionally tailored to match the observed statistical properties and correlation trends of the density profiles, the successful realization of a realistic ETG sample strongly indicates that the crucial processes which shape the total density profiles are implemented realistically within the simulation prescription, notwithstanding certain systematic biases.

Thus with such a realistic sample of IllustrisTNG ETGs, we can trace these ETGs to high redshift and further study the key physical processes (including merger events, AGN feedback, star formation activities etc.) relevant for the formation and evolution of the isothermal density profiles. A more detailed stellar mass-dependent redshift evolution comparison of γ' of the statistical sample and the main branch progenitor sample will further constrain the sample biases in the slope evolutionary trend. These will be presented in a follow-up paper (Paper II, Wang et al. in preparation).

ACKNOWLEDGEMENTS

We thank Daniel Eisenstein, Dylan Nelson, Peter Schneider, Rhea-Silvia Remus, Ryan McKinnon and Stephanie O'Neil for helpful discussions and support during the preparation of this paper. YW would like to thank the Tsinghua Xuetang Talents Program for funding his research at MIT. MV acknowledges support through an MIT RSC award, a Kavli Research Investment Fund, NASA ATP grant NNX17AG29G, and NSF grants AST-1814053 and AST-1814259. DX would like to thank the supercomputing facilities at the Heidelberg Institute for Advanced Studies and the Klaus Tschira Foundation. This work is partly supported by the National Key Basic Research and Development Program of China (No. 2018YFA0404501 to SM), and by the National Science Foundation of China (Grant No. 11333003, 11390372 and 11761131004 to SM).

REFERENCES

Abadi M. G., Navarro J. F., Fardal M., Babul A., Steinmetz M., 2010, MNRAS, 407, 435

Auger M. W., Treu T., Bolton A. S., Gavazzi R., Koopmans L. V. E., Marshall P. J., Bundy K., Moustakas L. A., 2009, ApJ, 705, 1099

Auger M. W., Treu T., Gavazzi R., Bolton A. S., Koopmans L. V. E., Marshall P. J., 2010a, ApJ, 721, L163

Auger M. W., Treu T., Bolton A. S., Gavazzi R., Koopmans L. V. E., Marshall P. J., Moustakas L. A., Burles S., 2010b, ApJ, 724, 511

Barber C., Crain R. A., Schaye J., 2018, MNRAS, 479, 5448

Barnabè M., Czoske O., Koopmans L. V. E., Treu T., Bolton A. S., Gavazzi R., 2009, MNRAS, 399, 21

Barnabè M., Czoske O., Koopmans L. V. E., Treu T., Bolton A. S., 2011, MNRAS, 415, 2215

Barnes D. J., et al., 2018, MNRAS,

Baugh C. M., Cole S., Frenk C. S., Benson A. J., Lacey C. G., 1999, in Carral P., Cepa J., eds, Astronomical Society of the Pacific Conference Series Vol. 163, Star Formation in Early Type Galaxies. p. 227 (arXiv:astro-ph/9808209)

Bellstedt S., et al., 2018, MNRAS, 476, 4543

Bernardi M., Meert A., Vikram V., Huertas-Company M., Mei S., Shankar F., Sheth R. K., 2012, preprint, (arXiv:1211.6122)

Binney J., Tremaine S., 2008, Galactic Dynamics: Second Edition. Princeton University Press

Blumenthal G. R., Faber S. M., Primack J. R., Rees M. J., 1984, Nature, 311, 517

Blumenthal G. R., Faber S. M., Flores R., Primack J. R., 1986, ApJ, 301, 27

Bolton A. S., Burles S., Koopmans L. V. E., Treu T., Moustakas L. A., 2006, ApJ, 638, 703

Bolton A. S., Burles S., Koopmans L. V. E., Treu T., Gavazzi R., Moustakas L. A., Wayth R., Schlegel D. J., 2008, ApJ, 682, 964

Bolton A. S., et al., 2012, ApJ, 757, 82

Brodie J. P., et al., 2014, ApJ, 796, 52

Brownstein J. R., et al., 2012, ApJ, 744, 41

Bruderer C., Read J. I., Coles J. P., Leier D., Falco E. E., Ferreras I., Saha P., 2016, MNRAS, 456, 870

Bruzual G., Charlot S., 2003, MNRAS, 344, 1000

Cabanac R. A., et al., 2007, A&A, 461, 813

Cappellari M., 2008, MNRAS, 390, 71

Cappellari M., et al., 2006, MNRAS, 366, 1126

Cappellari M., et al., 2011, MNRAS, 413, 813

Cappellari M., et al., 2013a, MNRAS, 432, 1709

Cappellari M., et al., 2013b, MNRAS, 432, 1862

Chabrier G., 2003, PASP, 115, 763

Chua K. T. E., Pillepich A., Rodriguez-Gomez V., Vogelsberger M., Bird S., Hernquist L., 2017, MNRAS, 472, 4343

Chua K. E., Pillepich A., Vogelsberger M., Hernquist L., 2018, preprint, (arXiv:1809.07255)

Ciotti L., van Albada T. S., 2001, ApJ, 552, L13

Cole S., Aragon-Salamanca A., Frenk C. S., Navarro J. F., Zepf S. E., 1994, MNRAS, 271, 781

Cole S., Lacey C. G., Baugh C. M., Frenk C. S., 2000, MNRAS, 319, 168

Crain R. A., et al., 2015, MNRAS, 450, 1937

Davis M., Efstathiou G., Frenk C. S., White S. D. M., 1985, ApJ, 292, 371

Dolag K., Borgani S., Murante G., Springel V., 2009, MNRAS, 399, 497

Dubinski J., 1994, ApJ, 431, 617

Dubois Y., Gavazzi R., Peirani S., Silk J., 2013, MNRAS, 433, 3297

Dubois Y., et al., 2014, MNRAS, 444, 1453

Duffy A. R., Schaye J., Kay S. T., Dalla Vecchia C., 2008, MNRAS, 390, L64

Duffy A. R., Schaye J., Kay S. T., Dalla Vecchia C., Battye R. A., Booth C. M., 2010, MNRAS, 405, 2161

Dutton A. A., Macciò A. V., 2014, MNRAS, 441, 3359

Dutton A. A., Treu T., 2014, MNRAS, 438, 3594

Faber S. M., Dressler A., Davies R. L., Burstein D., Lynden Bell D., Terlevich R., Wegner G., 1987, in Faber S. M., ed., Nearly Normal Galaxies. From the Planck Time to the Present. pp 175–183

Forbes D. A., Alabi A., Romanowsky A. J., Brodie J. P., Strader J., Usher C., Pota V., 2016, MNRAS, 458, L44

Gao L., Navarro J. F., Cole S., Frenk C. S., White S. D. M., Springel V., Jenkins A., Neto A. F., 2008, MNRAS, 387, 536

Gavazzi R., Treu T., Marshall P. J., Brault F., Ruff A., 2012, ApJ, 761, 170

Genel S., et al., 2014, MNRAS, 445, 175

Genel S., et al., 2018, MNRAS, 474, 3976

Gnedin O. Y., Kravtsov A. V., Klypin A. A., Nagai D., 2004, ApJ, 616, 16

Governato F., et al., 2010, Nature, 463, 203

Graham A. W., 2008, ApJ, 680, 143

Grillo C., 2012, ApJ, 747, L15

Hirschmann M., et al., 2013, MNRAS, 436, 2929

Hirschmann M., Dolag K., Saro A., Bachmann L., Borgani S., Burkert A., 2014, MNRAS, 442, 2304

Hirschmann M., Naab T., Ostriker J. P., Forbes D. A., Duc P.-A., Davé R., Oser L., Karabal E., 2015, MNRAS, 449, 528

Hjorth J., Williams L. L. R., Wojtak R., McLaughlin M., 2015, ApJ, 811, 2

Hopkins P. F., Cox T. J., Younger J. D., Hernquist L., 2009, ApJ, 691, 1168

Humphrey P. J., Buote D. A., 2010, MNRAS, 403, 2143

Humphrey P. J., Buote D. A., Gastaldello F., Zappacosta L., Bullock J. S., Brighenti F., Mathews W. G., 2006, ApJ, 646, 899

Johansson P. H., Naab T., Ostriker J. P., 2012, ApJ, 754, 115

Jorgensen I., Franx M., Kjaergaard P., 1996, MNRAS, 280, 167

Kauffmann G., White S. D. M., Guiderdoni B., 1993, MNRAS, 264, 201

Koopmans L. V. E., Treu T., 2003, ApJ, 583, 606

Koopmans L. V. E., Treu T., Bolton A. S., Burles S., Moustakas L. A., 2006, ApJ, 649, 599

Koopmans L. V. E., et al., 2009, ApJ, 703, L51

Kormendy J., Fisher D. B., Cornell M. E., Bender R., 2009, ApJS, 182, 216

La Barbera F., de Carvalho R. R., de La Rosa I. G., Lopes P. A. A., Kohl-Moreira J. L., Capelato H. V., 2010, MNRAS, 408, 1313

Li H., et al., 2017, ApJ, 838, 77

Lovell M. R., et al., 2018, MNRAS, 481, 1950

Lyskova N., Churazov E., Naab T., 2018, MNRAS, 475, 2403

Ma C.-P., Greene J. E., McConnell N., Janish R., Blakeslee J. P., Thomas J., Murphy J. D., 2014, ApJ, 795, 158

Macciò A. V., Dutton A. A., van den Bosch F. C., Moore B., Potter D., Stadel J., 2007, MNRAS, 378, 55

Madau P., Dickinson M., 2014, ARA&A, 52, 415

Marinacci F., et al., 2018, MNRAS, 480, 5113

McConnell N. J., Ma C.-P., 2013, ApJ, 764, 184

Naab T., Johansson P. H., Ostriker J. P., Efstathiou G., 2007, ApJ, 658, 710

Naab T., Johansson P. H., Ostriker J. P., 2009, ApJ, 699, L178

Naiman J. P., et al., 2018, MNRAS, 477, 1206

Navarro J. F., Frenk C. S., White S. D. M., 1997, ApJ, 490, 493

Navarro J. F., et al., 2010, MNRAS, 402, 21

Nelson D., et al., 2015, Astronomy and Computing, 13, 12

Nelson D., et al., 2018, MNRAS, 475, 624

Neto A. F., et al., 2007, MNRAS, 381, 1450

Newman A. B., Treu T., Ellis R. S., Sand D. J., 2013, ApJ, 765, 25

Newman A. B., Ellis R. S., Treu T., 2015, ApJ, 814, 26

Nipoti C., Treu T., Bolton A. S., 2009a, ApJ, 703, 1531

Nipoti C., Treu T., Auger M. W., Bolton A. S., 2009b, ApJ, 706, L86

Oñorbe J., Garrison-Kimmel S., Maller A. H., Bullock J. S., Rocha M., Hahn O., 2014, MNRAS, 437, 1894
Oguri M., Rusu C. E., Falco E. E., 2014, MNRAS, 439, 2494
Oldham L. J., Auger M. W., 2018, MNRAS, 476, 133
Oser L., Ostriker J. P., Naab T., Johansson P. H., Burkert A., 2010, ApJ, 725, 2312
Oser L., Naab T., Ostriker J. P., Johansson P. H., 2012, ApJ, 744, 63
Pillepich A., et al., 2018a, MNRAS, 473, 4077
Pillepich A., et al., 2018b, MNRAS, 475, 648
Pinkney J., et al., 2003, ApJ, 596, 903
Planck Collaboration et al., 2016, A&A, 594, A13
Poci A., Cappellari M., McDermid R. M., 2017, MNRAS, 467, 1397
Remus R.-S., Burkert A., Dolag K., Johansson P. H., Naab T., Oser L., Thomas J., 2013, ApJ, 766, 71
Remus R.-S., Dolag K., Naab T., Burkert A., Hirschmann M., Hoffmann T. L., Johansson P. H., 2017, MNRAS, 464, 3742
Robertson B., Cox T. J., Hernquist L., Franx M., Hopkins P. F., Martini P., Springel V., 2006a, ApJ, 641, 21
Robertson B., Hernquist L., Cox T. J., Di Matteo T., Hopkins P. F., Martini P., Springel V., 2006b, ApJ, 641, 90
Rodriguez-Gomez V., et al., 2015, MNRAS, 449, 49
Rodriguez-Gomez V., et al., 2016, MNRAS, 458, 2371
Ruff A. J., Gavazzi R., Marshall P. J., Treu T., Auger M. W., Brault F., 2011, ApJ, 727, 96
Schaller M., et al., 2015a, MNRAS, 451, 1247
Schaller M., et al., 2015b, MNRAS, 452, 343
Schaye J., et al., 2015, MNRAS, 446, 521
Serra P., Oosterloo T., Cappellari M., den Heijer M., Józsa G. I. G., 2016, MNRAS, 460, 1382
Sérsic J. L., 1963, Boletin de la Asociacion Argentina de Astronomia La Plata Argentina, 6, 41
Shankar F., et al., 2017, ApJ, 840, 34
Shen S., Mo H. J., White S. D. M., Blanton M. R., Kauffmann G., Voges W., Brinkmann J., Csabai I., 2003, MNRAS, 343, 978
Sijacki D., Vogelsberger M., Genel S., Springel V., Torrey P., Snyder G. F., Nelson D., Hernquist L., 2015, MNRAS, 452, 575
Sonnenfeld A., Treu T., Gavazzi R., Marshall P. J., Auger M. W., Suyu S. H., Koopmans L. V. E., Bolton A. S., 2012, ApJ, 752, 163
Sonnenfeld A., Treu T., Gavazzi R., Suyu S. H., Marshall P. J., Auger M. W., Nipoti C., 2013, ApJ, 777, 98
Sonnenfeld A., Nipoti C., Treu T., 2014, ApJ, 786, 89
Sonnenfeld A., Treu T., Marshall P. J., Suyu S. H., Gavazzi R., Auger M. W., Nipoti C., 2015, ApJ, 800, 94
Springel V., 2010, MNRAS, 401, 791
Springel V., White S. D. M., Tormen G., Kauffmann G., 2001, MNRAS, 328, 726
Springel V., et al., 2005, Nature, 435, 629
Springel V., et al., 2018, MNRAS, 475, 676
Teklu A. F., Remus R.-S., Dolag K., Beck A. M., Burkert A., Schmidt A. S., Schulze F., Steinborn L. K., 2015, ApJ, 812, 29
Thomas J., Saglia R. P., Bender R., Thomas D., Gebhardt K., Magorrian J., Corsini E. M., Wegner G., 2007, MNRAS, 382, 657
Torrey P., Vogelsberger M., Genel S., Sijacki D., Springel V., Hernquist L., 2014, MNRAS, 438, 1985
Torrey P., et al., 2017, preprint, (arXiv:1711.05261)
Torrey P., et al., 2018, MNRAS, 477, L16
Tortora C., La Barbera F., Napolitano N. R., Romanowsky A. J., Ferreras I., de Carvalho R. R., 2014, MNRAS, 445, 115
Treu T., Koopmans L. V. E., 2002, ApJ, 575, 87
Treu T., Koopmans L. V. E., 2004, ApJ, 611, 739
Treu T., Koopmans L. V., Bolton A. S., Burles S., Moustakas L. A., 2006, ApJ, 640, 662
Treu T., Auger M. W., Koopmans L. V. E., Gavazzi R., Marshall P. J., Bolton A. S., 2010, ApJ, 709, 1195
Vogelsberger M., Genel S., Sijacki D., Torrey P., Springel V., Hernquist L., 2013, MNRAS, 436, 3031
Vogelsberger M., et al., 2014a, MNRAS, 444, 1518
Vogelsberger M., et al., 2014b, Nature, 509, 177
Vogelsberger M., et al., 2018, MNRAS, 474, 2073
Wasserman A., et al., 2018, ApJ, 863, 130
Weinberger R., et al., 2017, MNRAS, 465, 3291
White S. D. M., Rees M. J., 1978, MNRAS, 183, 341
Xu D., Sluse D., Schneider P., Springel V., Vogelsberger M., Nelson D., Hernquist L., 2016, MNRAS, 456, 739
Xu D., Springel V., Sluse D., Schneider P., Sonnenfeld A., Nelson D., Vogelsberger M., Hernquist L., 2017, MNRAS, 469, 1824
Zhao H., 1996, MNRAS, 278, 488
de Vaucouleurs G., 1948, Annales d'Astrophysique, 11, 247
van der Wel A., et al., 2014, ApJ, 788, 28

APPENDIX A: COMPARISON DATASETS OF THE POWER-LAW PROFILES

In this section we give a more detailed documentation of the datasets we used for the comparison of the different slope correlation trends with the IllustrisTNG ETGs in Section 3. The dynamic modeling dataset of local ETGs is given in the upper half of Table A1, while the strong lensing dataset of higher redshift ETGs is given in the lower half of Table A1. The simulation dataset is given in Table A2. For each study, its parent survey or simulation, the sample redshift z, the definition of the total density slope γ', the assumed initial mass function (IMF), the specifications of stellar kinematics, the aperture size in which the central dark matter fraction $f_{\rm DM}$ is calculated, the mean of the slope $\langle\gamma'\rangle$ and the scatter of the slope $\sigma_{\gamma'}$ are given in the tables. We note that the total density slope for the strong lensing dataset is inferred from joint lensing and dynamics analysis, constrained by the total mass enclosed within the lens Einstein radius $M_{\rm Ein}$, the aperture velocity dispersion $\sigma_{\rm apt}$, and the de Vaucouleurs fit to the lens light profile.

APPENDIX B: COMPARISON DATASETS OF THE DARK MATTER INNER SLOPES

In this section we give a more detailed documentation of the datasets we used for the comparison of the dark matter profiles with the IllustrisTNG ETGs in Section 4. The observation and simulation datasets are given together in Table B1. For each study, its parent survey or simulation, the sample redshift z, the definition of the dark matter profile slope Γ', the sample halo mass M_{200}, the mean of the slope $\langle\Gamma'\rangle$ and the scatter of the slope $\sigma_{\Gamma'}$ are given in the table.

This paper has been typeset from a TEX/LATEX file prepared by the author.

Paper	Survey	z	γ' definition	IMF	Stellar kinematics	$f_{\rm DM}$ aperture	$\langle\gamma'\rangle$	$\sigma_{\gamma'}$
Thomas et al. (2007)	–	≈ 0	Logarithmic potential, best-fit within $R_{\rm eff}$	Constant M/L	Luminosity weighted stellar orbits with anisotropy	$r \leqslant R_{\rm eff}$	1.95	0.26
Tortora et al. (2014)	SPIDER+ ATLAS$^{\rm 3D}$	< 0.1	Mass-weighted slope at $R_{\rm eff}$	Variable	Two-component model for velocity dispersion, $\beta =$ 0.1 or 0.2	$r \leqslant R_{\rm eff}$	–	–
Serra et al. (2016)	ATLAS$^{\rm 3D}$	< 0.006	HI circular velocity averaged slope within $R_{\rm HI}$ ($4\,R_{\rm eff} - 16\,R_{\rm eff}$)	JAM modeling $M/L_r^{\rm JAM}$	Velocity dispersion projected within $R_{\rm eff}$	–	2.18 ± 0.03	0.11
Poci et al. (2017)	ATLAS$^{\rm 3D}$	< 0.01	Mean power-law slope on $[0.1\,R_{\rm eff}, R_{\rm eff}]$ (constrained data)	Salpeter	IFU, JAM modeling with variable anisotropy, velocity dispersion within $R_{\rm eff}$	$r \leqslant R_{\rm eff}$	2.193 ± 0.016	0.168 ± 0.015
Bellstedt et al. (2018)	SLUGGS	< 0.005	Power-law slope on $[0.1\,R_{\rm eff}, 4\,R_{\rm eff}]$	Constant M/L	JAM modeling with variable anisotropy, velocity dispersion within $R_{\rm eff}$	$r \leqslant R_{\rm eff}$ (Poci et al. 2017 model III)	2.12 ± 0.05	–
Treu & Koopmans (2004)	LSD	[0.5, 1.0]	Power-law slope within $R_{\rm Ein}$	Joint lensing and dynamics M/L	$\sigma_{\rm SIE}$, Osipkov-Merritt anistropy/ constant $\beta(r)$	$r \leqslant R_{\rm Ein}$	1.75 ± 0.10	0.2
Koopmans et al. (2006)	SLACS	[0.06, 0.33]	Power-law slope within $R_{\rm Ein}$	Constant $M/L_{\rm B}$	LOS velocity dispersion, variable anisotropy	$r \leqslant R_{\rm Ein}$	$2.01^{+0.02}_{-0.03}$	0.12
Auger et al. (2010b)	SLACS	[0.24, 0.78]	Power-law slope	Chabrier/ Salpeter	Velocity dispersion within $R_{\rm eff}/2$, $\beta = 0$	$r \leqslant R_{\rm eff}/2$	2.078 ± 0.027	0.16 ± 0.02
Barnabè et al. (2011)	SLACS	[0.08, 0.33]	Axisymmetric power-law slope	Chabrier/ Salpeter	Axisymmetric model, two-integral Schwarzschild model	$r \leqslant R_{\rm eff}$	$2.074^{+0.043}_{-0.041}$	$0.144^{+0.055}_{-0.014}$
Ruff et al. (2011)	SL2S	[0.24, 0.77]	Power-law slope within $R_{\rm Ein}$	Salpeter	Velocity dispersion within $R_{\rm Ein}$, $\beta = 0$	$r \leqslant R_{\rm eff}/2$ (projected 2D)	$2.16^{+0.16}_{-0.16}$	$0.25^{+0.10}_{-0.07}$
Sonnenfeld et al. (2013)	SL2S	[0.2, 0.8]	Power-law slope within $R_{\rm Ein}$	Salpeter	Velocity dispersion within $R_{\rm Ein}$, $\beta = 0$	–	$2.05^{+0.06}_{-0.06}$	$0.14^{+0.04}_{-0.03}$

Table A1. The observational datasets of ETGs analyzed by dynamic modeling and strong lensing surveys utilized for comparison in Section 3. The dynamic modeling dataset of local ETGs is given in the upper half of the table, while the strong lensing dataset of higher redshift ETGs is given in the lower half of the table. For each study, its parent survey, the sample redshift z, the definition of the total density slope γ', the assumed initial mass function (IMF), the specifications of stellar kinematics, the aperture size in which the central dark matter fraction $f_{\rm DM}$ is calculated, the mean of the slope $\langle\gamma'\rangle$ and the scatter of the slope $\sigma_{\gamma'}$ are given in the table. We note that the total density slope for the strong lensing dataset is inferred from joint lensing and dynamics analysis, constrained by the total mass enclosed within the lens Einstein radius $M_{\rm Ein}$, the aperture velocity dispersion $\sigma_{\rm apt}$, and the de Vaucouleurs fit to the lens light profile. A '–' is assigned to any field that is not applicable.

Paper	Simulation	z	γ' definition	IMF	Stellar kinematics	$f_{\rm DM}$ aperture	$\langle\gamma'\rangle$	$\sigma_{\gamma'}$
Remus et al. (2017)	Magneticum (cosmological, with AGN, weak wind)	[0, 0.5, 1, 2]	Power-law slope	–	–	$r \leqslant R_{\rm eff}$	2.05	0.13
Remus et al. (2017)	Oser (zoom-in, no AGN, no wind)	[0, 0.5, 1, 2]	Power-law slope	–	–	$r \leqslant R_{\rm eff}$	2.30	0.28
Remus et al. (2017)	Wind (zoom-in, no AGN, strong wind)	[0, 0.5, 1, 2]	Power-law slope	–	–	$r \leqslant R_{\rm eff}$	2.56	0.03

Table A2. The simulation dataset of ETGs utilized for comparison in Section 3. For each paper, its parent simulation, the sample redshift z, the definition of the total density slope γ', the assumed initial mass function (IMF), the specifications of stellar kinematics, the aperture size in which the central dark matter fraction $f_{\rm DM}$ is calculated, the mean of the slope $\langle\gamma'\rangle$ and the scatter of the slope $\sigma_{\gamma'}$ are given in the table. A '–' is assigned to any field that is not applicable.

Paper	Survey/Simulation	z	Γ' definition	$\log M_{200}\,[M_\odot]$	$\langle\Gamma'\rangle$	$\sigma_{\Gamma'}$
Newman et al. (2015)	–	0.208	$\gamma'_{\rm DM}$ $(r \leqslant R_{\rm eff})$	[13.65, 14.45]	1.12	0.22
Sonnenfeld et al. (2015)	SL2S+SLACS	[0.24, 0.88]	gNFW inner slope	$13.44^{+0.16}_{-0.16}$	$0.80^{+0.18}_{-0.22}$	–
Oldham & Auger (2018)	–	0.185	gNFW inner slope	[11.04, 12.46]	1.62	0.61
Wasserman et al. (2018)	–	0.185	gNFW inner slope	$13.28^{+0.47}_{-0.28}$	$0.96^{+0.24}_{-0.41}$	–
Schaller et al. (2015b)	EAGLE	0.0	gNFW inner slope	[13.40, 14.11]	1.36	0.11

Table B1. The observational and simulation datasets of ETG dark matter density profiles utilized for comparison in Section 4. For each study, its parent survey or simulation, the sample redshift z, the definition of the dark matter profile slope Γ', the sample halo mass M_{200}, the mean of the slope $\langle\Gamma'\rangle$ and the scatter of the slope $\sigma_{\Gamma'}$ are given in the table. A '–' is assigned to any field that is not applicable.